IRAQI JOURNAL OF APPLIED PHYSICS

The *Iraqi Journal of Applied Physics (IJAP)* is a peer reviewed journal of high quality devoted to the publication of original research papers from applied physics and their broad range of applications. IJAP publishes quality original research papers, comprehensive review articles, survey articles, book reviews, dissertation abstracts in physics and its applications in the broadest sense. It is intended that the journal may act as an interdisciplinary forum for Physics and its applications. Innovative applications and material that brings together diverse areas of Physics are particularly welcome. Review articles in selected areas are published from time to time. It aims to disseminate knowledge; provide a learned reference in the field; and establish channels of communication between academic and research experts, policy makers and executives in industry, commerce and investment institutions. IJAP is a quarterly specialized periodical dedicated to publishing original papers, letters and reviews in: Applied & Nonlinear Optics, Applied Mechanics & Thermodynamics, Digital & Optical Communications, Electronic Materials & Devices, Laser Physics & Applications, Plasma Physics & Applications, Quantum Physics & Spectroscopy, Semiconductors & Optoelectronics, Solid State Physics & Applications, Alternative and Renewable Energy, and Computers and Networks.

ISSN (Print): 1813-2065, ISSN (Online): 2309-1673, ISSN (Letters): 1999-656X

EDITORIAL BOARD

Editorial Office:
P. O. Box 55259, Baghdad 12001, IRAQ
Website: www.iraqiphysicsjournal.com
Emails: info@iraqiphysicsjournal.com, editor_ijap@yahoo.co.uk, ijap.editor@gmail.com

ADVISORY BOARD

SPONSORED AND PUBLISHED BY
THE IRAQI SOCIETY FOR ALTERNATIVE AND RENEWABLE ENERGY SOURCES & TECHNIQUES (I.S.A.R.E.S.T.)

IRAQI JOURNAL OF APPLIED PHYSICS

ISSN (Print): 1813-2065, ISSN (Online): 2309-1673, ISSN (Letters): 1999-656X

INSTRUCTIONS TO AUTHORS

CONTRIBUTIONS

Contributions to be published in this journal should be original research works, i.e., those not already published or submitted for publication elsewhere, individual papers or letters to editor.
Manuscripts should be submitted to the editor at the mailing address:
Iraqi Journal of Applied Physics, Editorial Board, P. O. Box 55259, Baghdad 12001, IRAQ
Website: www.iraqiphysicsjournal.com
Email: editor@iraqiphysicsjournal.com, editor_ijap@yahoo.co.uk, ijap.editor@gmail.com

MANUSCRIPTS

Two hard copies with soft copy on a compact disc (CD) should be submitted to Editor in the following configuration:

- **One-column** Double-spaced one-side A4 size with 2.5 cm margins of all sides
- Times New Roman font (16pt bold for title, 14pt bold for names, 12pt bold for headings, 12pt regular for text)
- Letters should not exceed 10 pages, papers should not exceed 20 pages and reviews are up to author.
- Manuscripts presented in English only are accepted.
- English abstract not exceed 150 words
- 4 keywords (at least) should be maintained on (PACS preferred)
- Author(s) should express all quantities in SI units
- Equations should be written in equation form (*italic* and symbolic)
- Figures and Tables should be separated from text
- Figures and diagrams can be submitted in colors for assessment and they will be returned to authors after provide printable copies
- Charts should be indicated by the software used for
- Only original or high-resolution scanner photos are accepted
- For electronic submission, articles should be formatted with MS-Word software.

AUTHOR NAMES AND AFFILIATIONS

It is IJAP policy that all those who have participated significantly in the technical aspects of a paper be recognized as co-authors or cited in the acknowledgments. In the case of a paper with more than one author, correspondence concerning the paper will be sent to the first author unless staff is advised otherwise.
Author name should consist of first name, middle initial, last name. The author affiliation should consist of the following, as applicable, in the order noted:
- Company or college (with department name or company division), Postal address, City, state, zip code, Country name, contacting telephone, and e-mail

REFERENCES

The references should be brought at the end of the article, and numbered in the order of their appearance in the paper. The reference list should be cited in accordance with the following examples:
[1] X. Ning and M.R. Lovell, "On the Sliding Friction Characteristics of Unidirectional Continuous FRP Composites", *ASME J. Tribol.*, 124(1) (2002) 5-13.
[2] M. Barnes, "Stresses in Solenoids", *J. Appl. Phys.*, 48(5) (2001) 2000–2008.
[3] J. Jones, **"Contact Mechanics"**, Cambridge University Press (Cambridge, UK) (2000), Ch.6, p.56.
[4] Y. Lee, S.A. Korpela and R. Horne, "Structure of Multi-Cellular Natural Convection in a Tall Vertical Annulus", Proc. 7th International Heat Transfer Conference, U. Grigul et al., eds., Hemisphere (Washington DC), 2 (1982) 221–226.
[5] M. Hashish, "Waterjet Technology Development", High Pressure Technology, PVP-Vol. 406 (2000) 135-140.
[6] D.W. Watson, "Thermodynamic Analysis", ASME Paper No. 97-GT-288 (1997).
[7] C.Y. Tung, "Evaporative Heat Transfer in the Contact Line of a Mixture", Ph.D. thesis, Rensselaer Polytechnic Institute, Troy, NY (1982).

PROOFS

Authors will receive proofs of papers and are requested to return one corrected hard copy with a WORD copy on a compact disc (CD). New materials inserted in the original text without Editor permission may cause rejection of paper.

COPYRIGHT FORM

Author(s) will be asked to transfer copyrights of the article to the Journal soon after acceptance of it. This will ensure the widest possible dissemination of information.

OFFPRINTS

Authors will receive offprints free of charge and any additional reprints can be ordered.

SUBSCRIPTION AND ORDERS

Annual fees (4 issues per year) of subscription are:
50 US$ for individuals inside Iraq; **200** US$ for institutions inside Iraq;
100 US$ for individuals abroad; **300** US$ for institutions abroad.
Fees are reduced by 25% for I.S.A.R.E.S.T. members. Orders of issues can be submitted by contacting the editor-in-chief or editorial office at admin@iraqiphysicsjournal.com, or editor_ijap@yahoo.co.uk to maintain the address of issue delivery and payment way.

IRAQI JOURNAL OF APPLIED PHYSICS
Vol. 18, No. 1, January-March 2022, pp. 3-8

Fabrication of Solid Random Gain Media in Visible Region from Rhodamine Dye Solutions Containing Highly-Pure Titanium Dioxide Nanoparticles

Asal A. Moahmmed Ali
Mohammed A. Hameed

Department of Physics, College of Science, University of Baghdad, Baghdad, IRAQ

In this work, solid random gain media were fabricated from laser dye solutions containing nanoparticles as scattering centers. Two different rhodamine dyes (123 and 6G) were used to host the highly-pure titanium dioxide nanoparticles to form the random gain media. The spectroscopic characteristics (mainly fluorescence) of these media were determined and studied. These random gain media showed laser emission in the visible region of electromagnetic spectrum. Fluorescence characteristics can be controlled to few nanometers by adjusting the characteristics of the host and nanoparticles as well as the preparation conditions of the samples. Emission of narrow linewidth (3nm) and high intensity in the visible region (533-537nm) was obtained.

Keywords: Random gain media; Laser dyes; Rhodamine 6G; Nanoparticles
Received: 28 December 2021; **Revised:** 28 January 2022; **Accepted:** 05 February 2022

1. Introduction

Since the invention of the first laser in 1960, one of the most fundamental challenges in laser physics is the fabrication of high-efficiency laser system [1,2]. Recently, the research on the multiple scattering by tiny particles within random gain medium and has led to a new field known as “random lasers”, which generate coherent light with no need to conventional laser resonator as the light amplification is obtained by the multiple scattering of photons in such amplifying disordered medium [3-6]. This process is governed by the Rayleigh condition of scattering as $\lambda >> d$, where d is the diameter of the particle at which the photon is scattered.

The need for laser emission at certain wavelength is increasing as the uses and applications of lasers are drastically increasing. This could be carried out using optical or optoelectronic elements added inside the laser resonator to control the emitted wavelength or to select certain wavelength from the output laser linewidth [7-9]. Random laser can acceptably produce the output with single wavelength. This mainly depends on the selection of the host medium (dye) containing the scattering particles (scatterers) and their spectral properties [10]. The idea of the random gain medium is mainly based on the presence of small particles inside the gain medium, so they will act as random and multiple scattering centers [11,12]. The scattering centers will act as tiny resonators inside the dyes medium to achieve the required amplification of laser signal [13-16].

Organic dyes have been used as gain medium for lasers since the 1960s, long before the invention of today’s organic electronic devices [1]. Organic gain materials are highly attractive for lasing due to their chemical tunability and large stimulated emission cross section [15]. When the organic dye is dissolved in a suitable solvent (such as ethanol, methanol, water, etc.), it can be used easily as laser active medium in dye lasers [16].

Among all laser dyes, Rhodamine 6G (also known as R590) is the most common and frequently used for laser generation due to its high efficiency in addition to the wide tunable spectral bandwidth [17]. As it has a large cross-section area compared to other dyes and its high photo-stability, this dye has a high absorption in the visible range [18]. The molecular structure of this dye is characterized by a number of double bonds assigned as "π-bond coupling", which is the reason for the activity of such materials [19,20]. However, the family of xanthene dyes including fluorescein, eosin and rhodamines, the latter show the higher quantum efficiencies in photonic and optoelectronic uses [21].

In this work, solid random gain media were fabricated from laser dye solutions containing nanoparticles as scattering centers. Two different rhodamine dyes (123 and 6G) were used to host the highly-pure titanium dioxide nanoparticles to form the random gain media. The spectroscopic characteristics (mainly fluorescence) of these media were determined and studied. These random gain media showed laser emission in the visible region of

electromagnetic spectrum. These characteristics (mainly emission wavelength to few nanometers) can be controlled by adjusting the characteristics of the host and nanoparticles. Emission of narrow linewidth and high intensity in the visible region was obtained.

2. Experimental Method

Rhodamine 123 and Rhodamine 6G dyes (supplied by Lambda Physik) were used in this work as the host media. The dye solutions were prepared by dissolving different molar concentrations of each dye (10^{-2}, 10^{-3}, 10^{-4}, $5x10^{-4}$, 10^{-5}, $5x10^{-5}$, 10^{-6} M) in different solvents (ethanol, methanol, propanol, hexanol, chloroform, distilled water, acetone) to determine the optimum concentrations as well optimum solvents.

According to the absorption and fluorescence spectra of the prepared solutions recorded in the spectral range 170-960 nm, it was found that the optimum molar concentration was 10^{-4} M for Rhodamine 123 in propanol and 10^{-5} M for Rhodamine 6G in propanol too.

Different weights (0.5, 1, 1.5, 2 and 2.5 mg) of highly-pure titanium dioxide nanoparticles were added to the prepared solutions to form random gain media. The solution was slowly stirred to ensure the homogeneous diffusion of the nanoparticles within the dye solution. The optimum weight of these nanoparticles was determined according to the fluorescence spectra as the weight corresponding to the sample exhibiting the highest fluorescence intensity.

A computer-controlled K-MAC Spectra Academy SV-2100 UV-visible spectrophotometer was used to record the fluorescence spectra of the prepared samples. Also, the fluorescence spectra were recorded using F96 Shanghai Leng Guang Fluorescence Spectrophotometer with a xenon lamp as the excitation source in the spectral range of 4500-650 nm. To measure the irradiance of the prepared samples, the light source of the spectrophotometer may be replaced with a laser source. The fluorescence measurements on the final samples in the solid form were performed by illuminating them with a 532nm laser in dark. This laser was maintained on a fixed holder to be aligned vertically and horizontally with respect to the sample.

The highly-pure titanium dioxide nanoparticles were synthesized by a dc reactive magnetron sputtering technique. The system used for this purpose is shown in Fig. (1a). A highly-pure titanium target was sputtered by plasma generated by argon discharge in presence of oxygen as reactive gas. The mixing ratio of Ar:O_2 gases was 50:50. More details on this technique can be found elsewhere [22-25].

Titanium dioxide thin films were deposited on glass substrates and the film thickness could be determined by the deposition time. The titanium dioxide nanoparticles (Fig. 1b) were extracted from the deposited thin films by the conjunctional freezing-assisted ultrasonic extraction technique. In this technique, the nanoparticles are extracted from the thin film without any heat treatment or mechanical processing and hence no increase in the particle size is induced. Experimental details on this technique can be found in references [26,27].

(a)

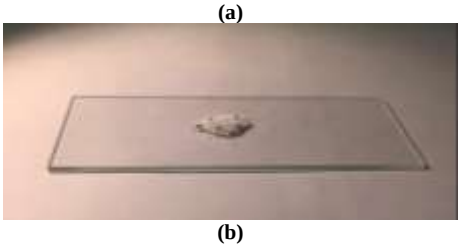

(b)

Fig. (1) (a) A photograph of the dc reactive magnetron sputtering system used in this work, and (b) the highly-pure TiO_2 nanopowder extracted from the thin film samples prepared in this work

As shown in Fig. (2a), the sample on the right was prepared from 10^{-4} M of Rhodamine 123 dye dissolved in propanol, while the sample on the left was prepared from 10^{-4} M of Rhodamine 123 dye dissolved in propanol and containing 2.5 mg of highly-pure TiO_2 nanoparticles. Similarly, as shown in Fig. (2b), the sample on the right was prepared from 10^{-5} M of Rhodamine 6G dye dissolved in propanol, while the sample on the left was prepared from 10^{-5} M of Rhodamine 6G dye dissolved in propanol and containing 2.5 mg of highly-pure TiO_2 nanoparticles.

Figure (3) shows the final samples of the random gain media fabricated as solid rods of Rhodamine 123 (Fig. 3a) and Rhodamine 6G (Fig. 3b) dyes dissolved in propanol and containing 2.5mg of TiO_2 nanoparticles. These samples were embedded in appropriate resin to take their solid shape.

The solid rod was prepared manually without any chemical or heat treatment by adding a sufficient amount of the resin to the dye solution containing the nanoparticles in a glass tube. The weight percentage of resin was 99%, while the dye solution containing nanoparticles represented 1% only. This mixture was kept inside the tube and left in dark at room temperature for 48 hours to get its final form. In order not to affect the absorption and fluorescence characteristics of the prepared solution, the resin is totally transparent in the visible region. Although, the fact that the nanoparticles might precipitate at the

bottom of the glass tube, the measurements confirmed that the nanoparticles were randomly distributed in the solid medium and their number was sufficiently large to perform multiple scattering.

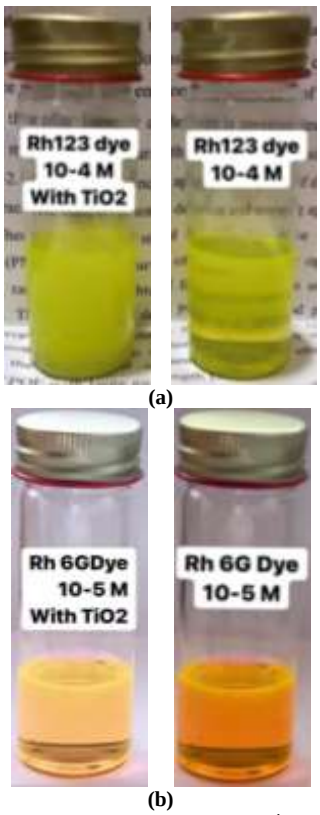

Fig. (2) The samples prepared from (a) 10^{-4} M of Rhodamine 123 dye dissolved in propanol without and with 2.5mg of TiO_2 nanoparticles, and (b) 10^{-5} M of Rhodamine 6G dye dissolved in propanol without and with 2.5mg of TiO_2 nanoparticles

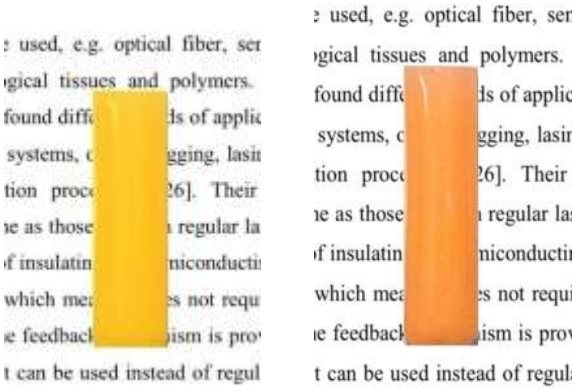

Fig. (3) The random gain media fabricated in this work as solid rods from 10^{-4} M of Rhodamine 123 (a) and Rhodamine 6G (b) dyes dissolved in propanol, containing 2.5mg of highly-pure TiO_2 nanoparticles and embedded in transparent resin

3. Results and Discussion

Figure (4) shows the x-ray diffraction (XRD) pattern of TiO_2 nanoparticles synthesized in this work using Ar:O_2 gas mixing ratio of 50:50 and after deposition time of 3 hours. The synthesized nanoparticles showed mixed-phase structure (anatase and rutile) of TiO_2. This pattern shows primarily the structural purity of the synthesized nanoparticles as no peaks belonging to other materials than TiO_2 were observed. The structural purity of the nanoparticles is very important to ensure the homogenous response of them as scattering centers to the laser signal generated by the dye hosting them.

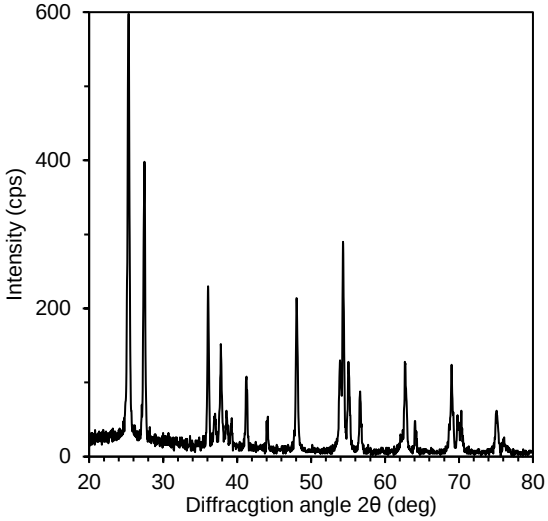

Fig. (4) XRD pattern for TiO_2 nanoparticles synthesized in this work

The formation of nanostructures in the prepared sample was identified by the SEM result as shown in Fig. (5). A minimum particle size of about 40 nm can be seen while no large aggregation is observed. Smooth and uniform morphology surface is observed with the presence of granular grains. The nanoparticles show alignment and homogeneous distribution (with no voids), but their diameters are rather uniform. The surface also contains polyhedral shells distributed randomly on the substrate, with some of them line up along the nanoparticles. These images also show small granular grains distributed throughout the surface without any cracks.

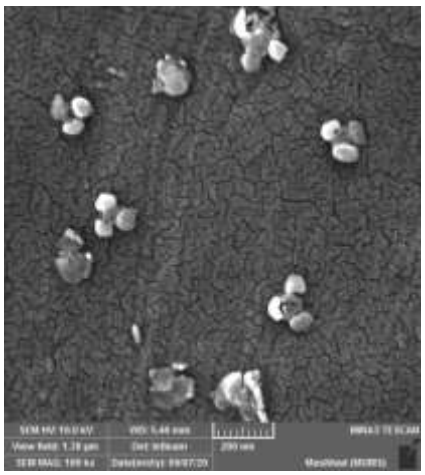

Fig. (5) The SEM image of the TiO_2 sample prepared in this work using 1:1 gas mixture after deposition time of 2 hours

In order to confirm the structural purity of the TiO_2 nanoparticles, which is highly preferred for studies concerned to the concepts of physical and chemical characteristics and processes, the energy-dispersive x-ray spectroscopy (EDX) was performed and its result is shown in Fig. (6). The elemental composition of TiO_2 nanoparticles shows that no elements other than Ti and O were found in the final sample and the stoichiometry of the TiO_2 compound is also confirmed.

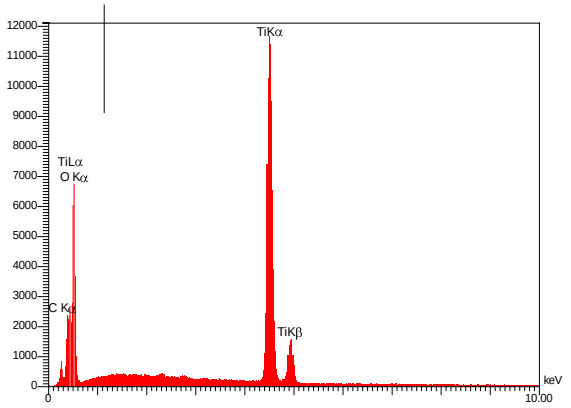

Fig. (6) EDX spectrum of TiO_2 nanoparticles synthesized in this work

Figure (7) shows the fluorescence spectra of the samples prepared from Rhodamine 123 dye in propanol before and after adding the TiO_2 nanoparticles in the spectral range of 450-650 nm using a 532nm laser beam as the excitation source. Similarly, figure (8) shows the fluorescence spectra of the samples prepared from Rhodamine 6G dye in propanol before and after adding the TiO_2 nanoparticles in the spectral range of 450-750nm using a 532nm laser beam as the excitation source.

For Rhodamine 123 samples, the peak intensity was measured in the narrow range 532-535 nm and the sample after adding the TiO_2 nanoparticles as a solid rod showed that the intensity is higher by 100% than that the peak intensity of the sample after adding the TiO_2 nanoparticles as a solution and by 250% than that of the dye solution only. Accordingly, the full-width at half maximum (FWHM) was determined to be 55 nm for Rhodamine 123 dye solution only, 12 nm for Rhodamine 123 dye solution with 2.5 mg of TiO_2 nanoparticles, and 3 nm for solid rod of Rhodamine 123 dye solution with 2.5 mg of TiO_2 nanoparticles.

In case of Rhodamine 6G samples, the peak intensity was measured in the narrow range 580-590 nm and the solid rod of Rhodamine 6G dye solution containing 2.5 mg of TiO_2 nanoparticles showed intensity higher by 100% than that of Rhodamine 6G dye solution containing 2.5 mg of TiO_2 nanoparticles and by 250% than Rhodamine 6G dye solution only. Accordingly, the full-width at half maximum (FWHM) was determined to be 60 nm for Rhodamine 6G dye solution only, 10 nm for Rhodamine 6G dye solution containing 2.5 mg of TiO_2 nanoparticles, and 4 nm for solid rod of Rhodamine 6G dye solution containing 2.5 mg of TiO_2 nanoparticles.

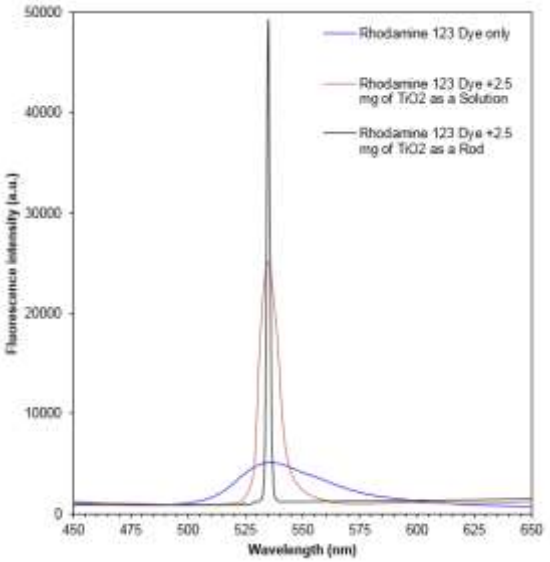

Fig. (7) Fluorescence spectra of solid samples prepared from Rhodamine 123 dye solution before and after adding TiO_2 nanoparticles using 532nm laser beam as the excitation source

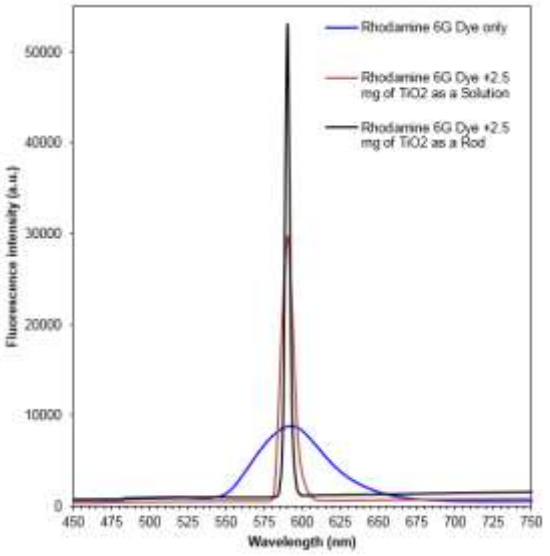

Fig. (8) Fluorescence spectra of solid samples prepared from Rhodamine 6G dye solution before and after adding TiO_2 nanoparticles using 532nm laser beam as the excitation source

Figure (9a) shows visually the fluorescence of the solid rod fabricated from Rhodamine 123 dye solution containing 2.5 mg of TiO_2 nanoparticles as it was irradiated with a 532 nm laser beam. It is apparent that the fluorescent volume of the sample is extending to more than 50 of the sample length. With a high intensity beam like laser, this is attributed to the homogeneous density of the sample. The fluorescence has a light yellowish green color, which lies within the spectral range of 530-565 nm. This experimental and direct result agrees well with the

precise measurement of fluorescence previously presented in Fig. (7), which is individually shown in Fig. (9b).

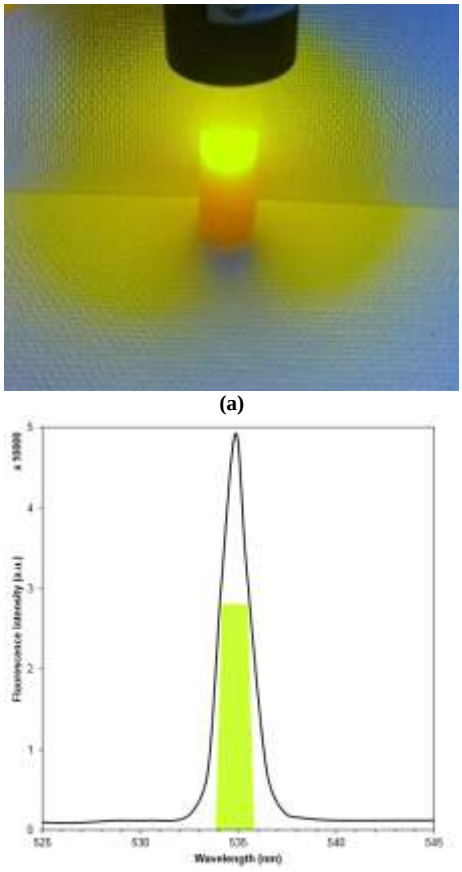

Fig. (9) (a) Fluorescence of the solid rod fabricated from Rhodamine 123 dye solution containing 2.5 mg of TiO_2 nanoparticles when irradiated by 532 nm laser beam, and (b) the position of experimental result within the spectral range of fluorescence presented in Fig. (5)

4. Conclusions

Random gain media were fabricated to produce laser radiation in the visible region of electromagnetic spectrum. These media were fabricated as solid rods from dye solutions hosting highly-pure nanoparticles. Two different rhodamine dyes (123 and 6G) were used to prepare solutions in propanol and host highly-pure titanium dioxide nanoparticles as scattering centers to form random gain media. These nanoparticles were synthesized by dc reactive magnetron sputtering technique and their structural purity were determined and found to have both phases of TiO_2 (anatase and rutile). This work represents a very encouraging attempt to fabricate highly-efficient and low-cost random lasers to emit in the visible region. Spectroscopic characteristics of the prepared samples showed that controlling preparation conditions can effectively control their fluorescence characteristics.

References

[1] M. Maeda, **"Laser Dyes, Properties of Organic for Dye Laser"**, Academic Press, Inc., (1984).
[2] W. Demtroder, **"Laser Spectroscopy"**, Springer-Verlag (New York, 1981), 330-350.
[3] S.K. Turitsyn et al., "Random distributed feedback fibre lasers", *Phys. Rep.*, 542(2) (2014) 133-193.
[4] H. Ramachandran, "Mirrorless lasers", *Pramana J. Phys.*, 58(2) (2002) 313.
[5] S. Wiersma, "The physics and applications of random lasers", *Nature Phys.*, 4 (2008) 359-365.
[6] D.V. Churkin et al., "Recent advances in fundamentals and applications of random fiber lasers", *Adv. Opt. Photon.*, 7 (2015) 516-569.
[7] P. Sebbah and C. Vanneste, "Random laser in the localized regime", *Phys. Rev. B*, 66 (2002) 144-202.
[8] J. Andreasen et al., "Modes of random lasers", *Adv. in Opt. Photon.*, 3(1) (2011) 88-127.
[9] R.C. Polson and Z.V. Vardeny, "Random lasing in dye-TiO_2 solution and π conjugated polymer films", *Phys. B*, 338 (2003) 219-223.
[10] B.K. Nasser and M.A. Hameed, "Narrow Emission Linewidth of Highly-Pure Silicon Nitride Nanoparticles in Different Dye Solutions as Random Gain Media", *Nonl. Opt. Quant. Opt.: Concepts in Modern Optics*, 53(1-2) (2021) 99-105.
[11] S. John and G. Pang, "Theory of Lasing in a Multiple Scattering Medium", *Phys. Rev. A*, 54(4) (1996) 3642.
[12] A. Ishimaru, **"Wave propagation and scattering in random media"**, Academic Press (New York, 1978) 175-183.
[13] M.A. Hameed, "Effects of Solvent Properties on Absorption and Fluorescence Characteristics of Two Organic Dyes Used as Random Gain Media", *Iraqi J. Appl. Phys.*, 17(2) (2021) 15-18.
[14] P. Sebbah, B. Hu and A.Z. Genack, "Speckle analysis of the microwave field in transmission through random media", *Proc. SPIE*, 6341 (2006), Speckle06: Speckles, From Grains to Flowers, 63411E.
[15] A.J.C. Kuehne and M.C. Gather, "Organic Lasers: Recent Developments on Materials, Device Geometries, and Fabrication Techniques", *Chem. Rev.*, 116(21) (2016) 12823-12864.
[16] F.J. Duarte, "Liquid and solid-state tunable organic dye lasers for medical applications", in **"Lasers for Medical Applications"**, Woodhead Publishing (2013) 203-221.
[17] J. Rietdorf, **"Microscopy Techniques",** Springer Berlin Heidelberg (2005).
[18] J. Kitur et al., "Dependence of the random laser behavior on the concentrations of dye and scatterers", *J. Opt.*, 12(2) (2010) 024009.
[19] A.A.R. Mahmood, O.A. Hammadi and K.R. Ibraheem, "Some Physical Properties of Metal-Hydroxyquinoline Complexes in Different Solvents", Iraqi J. Appl. Phys., 17(1) (2021) 9-16.
[20] H.G. Fahad and O.A. Hammadi, "Characterization of Highly-Pure Silicon Dioxide Nanoparticles as Scattering Centers for Random Gain Media", Iraqi J. Appl. Phys., 16(2) (2020) 37-42.

[21] D. Magde, R. Wong and P.G. Seybold, "Fluorescence Quantum Yields and Their Relation to Lifetimes of Rhodamine 6G and Fluorescein in Nine Solvents: Improved Absolute Standards for Quantum Yields", *Photochem. Photobio.*, 75(4) (2002) 327-334.
[22] F.J. Al-Maliki, O.A. Hammadi and E.A. Al-Oubidy, "Optimization of Rutile/Anatase Ratio in Titanium Dioxide Nanostructures prepared by DC Magnetron Sputtering Technique", *Iraqi J. Sci.*, 60(special issue) (2019) 91-98.
[23] F.J. Al-Maliki and E.A. Al-Oubidy, "Effect of gas mixing ratio on structural characteristics of titanium dioxide nanostructures synthesized by DC reactive magnetron sputtering", *Phys. B: Cond. Matter*, 555 (2019) 18-20
[24] R.A.H. Hassan and F.T. Ibrahim, "Preparation and Characterization of Anatase Titanium Dioxide Nanostructures as Smart and Self-Cleaned Surfaces", *Iraqi J. Appl. Phys.*, 16(4) (2020) 13-18.
[25] Mohammed A. Hameed, Saja H. Faisal, Reem H. Turki, "Characterization of Multilayer Highly-Pure Metal Oxide Structures Prepared by DC Reactive Magnetron Sputtering Technique", *Iraqi J. Appl. Phys.*, 16(4) (2020) 25-30
[26] O.A. Hammadi, "Production of Nanopowders from Physical Vapor Deposited Films on Nonmetallic Substrates by Conjunctional Freezing-Assisted Ultrasonic Extraction Method", *Proc. IMechE, Part N, J. Nanomater. Nanoeng. Nanosys.*, 232(4) (2018) 135-140.
[27] O.A. Hammadi, "Effects of Extraction Parameters on Particle Size of Titanium Dioxide Nanopowders Prepared by Physical Vapor Deposition Technique", Plasmonics, 15(6) (2020) 1747-1754.

IRAQI JOURNAL OF APPLIED PHYSICS
Vol. 18, No. 1, January-March 2022, pp. 9-14

Effects of Annealing and Substrate Temperatures on Dielectric Properties of $CuInGaS_2$ Structures Prepared by Quenching-Assisted Vacuum Coating Technique

Ahmed M. Elgebali
Emad S. Sami
Basma A. Moharram

Department of Power and Energy Engineering, Faculty of Engineering, Minia University, Menia, EGYPT

In this work, the effect of substrate temperature on some physical properties of $CuInGaS_2$ thin films was studied. The frequency and temperature dependencies upon AC conductivity were studied in the range 100Hz-10MHz and temperature range of 30-180°C. The AC activation energy was found to increase with increasing substrate temperature from 20 to 150°C and to decrease with increasing frequency from 100 Hz to 100 MHz. A nonsystematic sequence was shown with the increment of substrate temperature. According to these results, there is a strong relation between the preparation or substrate temperature and heat treatment as they have sufficient effects on the physical properties of the quaternary compound thin films.

Keywords: $CuInGaS_2$ semiconductor; Thin films; Heterojunction; Activation energy
Received: 12 October 2021; **Revised:** 22 January 2022; **Accepted:** 29 January 2022

1. Introduction

Recently, many quaternary materials have been extensively explored and invented for requiring a better performance of photonic and optoelectronic devices, such as $CuInGaS_2$, CuInGaSe, CuInSeTe, CuInSTe, ZnInSnO, InGaZnO, CuZnSnTe and Cu-ZnSnSe [1-8]. Particularly, $CuInGaS_2$ possesses Cu_2S and InGa characteristics that can be applied in many fields of photonics and optoelectronics [9]. This study uses multi-compound $CuInGaS_2$ material and applies in channel layer of thin-film transistors (TFTs). Many different Cu_2S-based TFTs became emerging devices and strongly expected to replace conventional silicon TFTs because of their good device performance, and potential for transparent and flexible active circuits [10,11]. However, the composition of Cu_2S-based crystallization is not stable enough that can affect the performance of TFTs. The additional indium and tin doping promoted a more stable equilibrium the $CuInGaS_2$ matrix that can help the performance of the optoelectronics devices improvement [12].

Quaternary compounds are considered as absorbing materials for solar cell applications. There are few data available about their bulk material properties [13-15] as well as thin films [16-19]. The available data refer that there is a strong dependence between their structure and preparation conditions, which may be due to the amorphous nature as well as the dependencies of their properties on the ambient conditions. The electrical and optical properties of $CuInGaS_2$, CuInGaSe, CuInSeTe and CuInSeS thin films were determined and studied [20,21].

$CuInGaS_2$ adopts the chalcopyrite structure similar to high-efficiency $CuInGaSe_2$. Despite the high photoconversion efficiency of 23.35% achieved using $CuInGaS_2$, the certified record PCE of pure sulfide solar cells remained limited to 15.5% thus far. Hence, determining the losses and their underlying origin is of paramount importance to improve the understanding and, consequently, the performance of pure sulfide $CuInGaS_2$ chalcopyrite [22]. A good solar absorber material requires an efficient generation of photocarriers followed by a sustained build-up of charge-carrier density [23]. The latter is directly correlated to quasi-Fermi level splitting (QFLS) and charge-carrier lifetime, often used to analyze the absorber quality [24,25]. Non-radiative recombination losses reduce the maximum achievable QFLS and lifetime, increasing photo-voltage deficit. The PCE for $CuInGaS_2$ has remained limited for a long time, mainly due to a large photo-voltage deficit. Moreover, rather low QFLS and short charge-carrier lifetimes (~hundreds of ps) are typically observed for $CuInGaS_2$. This implies significant non-radiative recombination in $CuInGaS_2$. The origin of non-radiative recombination lies in both bulk and interface (front and back-contact) defects [26-28].

This work presents the synthesis of quaternary alloy of $CuInGaS_2$ and then preparation of thin films at various substrate temperatures and point out the dependencies of dielectric and structural properties on deposition condition using relation between the preparation temperature and these properties.

2. Experimental Work

The alloys of $CuInGaS_2$ were prepared by quenching technique. The exact amount of high purity (99.99%) copper (Cu), indium (In), gallium (Ga) and sulfur (S) elements, in accordance with their percentages, are used. The mixed elements are sealed in evacuated (~10^{-3} Torr) quartz ampoule (25 cm in length and 8 mm internal diameter). Ampoules containing the elements were heated up to 1000 °C and frequently rocked at the highest temperature for 10 hours. The quenching was done in water immediately after taking out the ampoules from the furnace. Edward vacuum coating system was used to deposit $CuInGaS_2$ films at different substrate temperatures (30, 100 and 150 °C).

Aluminum electrodes with thickness of 200 nm were deposited on each adjacent surfaces of specimen by thermal evaporation technique under pressure of 10^{-5} Torr using an Edward E306A coating unit. The specimen was fixed in a holder and placed into a Heresies electronic temperature-controlled oven. High and low holder terminals are connected to a Hewlett-Packard HP4274A dielectric analyzer, the third holder terminal was connected to the earth. The dielectric parameters like total resistance (R_T), total capacitance (C_T) and dissipation factor (tanδ) were measured (in parallel mode) under certain frequency range 10^2-10^6 Hz. The AC conductivity (σ_{AC}) has been estimated from the obtained dielectric data using the following relation [29]:

$$\varepsilon_2 = \frac{\sigma_{AC}}{\varepsilon_0} \quad (1)$$

where the dielectric constants (ε_1 and ε_2) can be calculated using the following relation [29]:

$$\varepsilon_1 = \frac{C.t}{\varepsilon_0 A} \quad (2)$$

where C is the capacitance, ε_0 is the permittivity of free space, t is film thickness, is the angular frequency, A is the effective area for capacitance, and σ_{AC} is the AC conductivity given by [30]:

$$\sigma_{AC} = \omega \varepsilon_0 \varepsilon_1 \tan\delta \quad (3)$$

where tanδ is the dielectric tangent loss

The conductivity measured with an AC technique is given by [30]:

$$\sigma(\omega,T) = \sigma_{dc}(T) + a(T)\omega^S \quad (4)$$

The first term $\sigma_{dc}(T)$ in Eq. (5) is the direct current or DC conductivity, ω=0, conductivity, while the second term a(T) is the temperature-dependence factor and "s" is an exponent in the range 0<s<1. This equation estimates that if the first term is less than the second term, then $\sigma(\omega,T) \propto \omega^s$, so that the plot diagram of σ versus log(ω) is a straight line with slope s. While if the first term is larger than the second term (with increasing temperature), then the plot of σ versus ω in log scale should give a horizontal straight-line.

3. Results and Discussion

Figure (1) shows the SEM images of the as-deposited $CuInGaS_2$ thin films deposited on substrates of different temperatures (20, 100 and 150°C). It is clear that the particle size on the surface is decreasing with increasing substrate temperature. This can be attributed to the effect of substrate temperature to diffuse the deposited particles into smaller ones before finally deposit over the substrate. This reduction in the particle size may have reasonable effect on the physical properties of these films, mainly conductivity and dielectric constant. However, increasing substrate temperature should be carefully chosen to produce $CuInGaS_2$ thin films with required properties and characteristics for certain uses and applications.

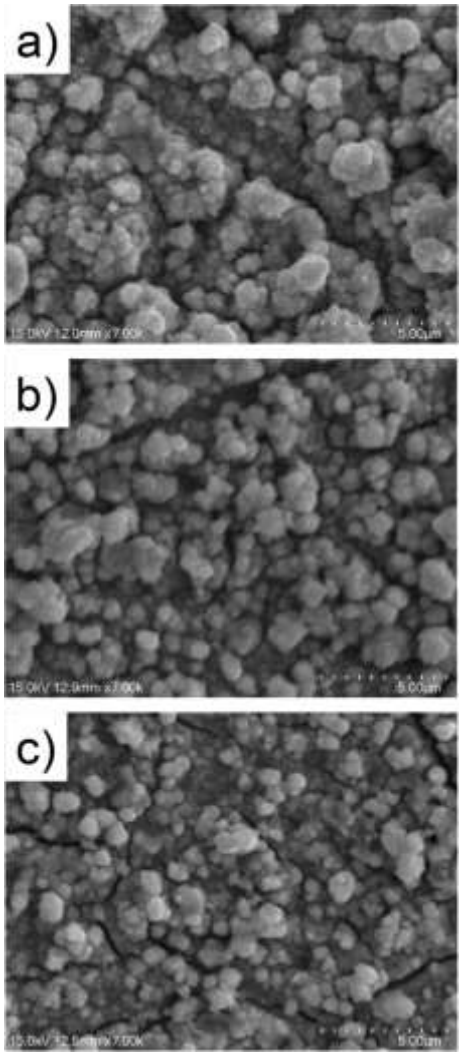

Fig. (1) SEM images of as-deposited $CuInGaS_2$ thin films deposited on substrates with temperature (a) 20°C, (b) 100°C, and (c) 150°C

Figure (2) shows the dependency of angular frequency on total conductivity $\sigma_{tot}(\omega)$ for the $CuInGaS_2$ thin films deposited at different substrate temperatures (20, 100 and 150°C) in the heat treatment range 30-180 °C. It is clear that there is proceeding increase of $\sigma_{tot}(\omega)$ that increased within the whole frequency range, i.e., the alternative (AC) conductivity, and the dominated or, σ_{DC} conductivity is much lesser than the σ_{AC}, which indicates that the

electronic polarization and the conductivity is purely AC. Some uses and applications of quaternary semiconducting thin films, especially power electronics and high-temperature photonics, require to determine such behavior within as much as stable range of varying temperatures.

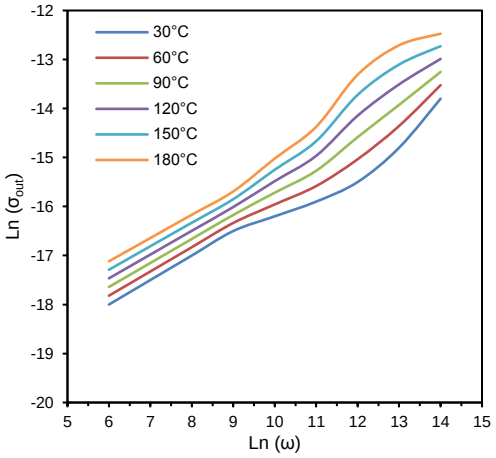

(a)

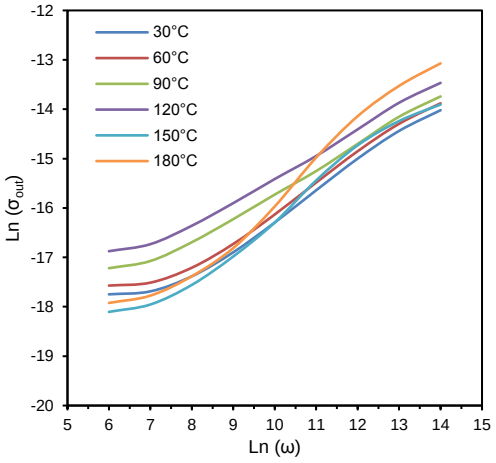

(b)

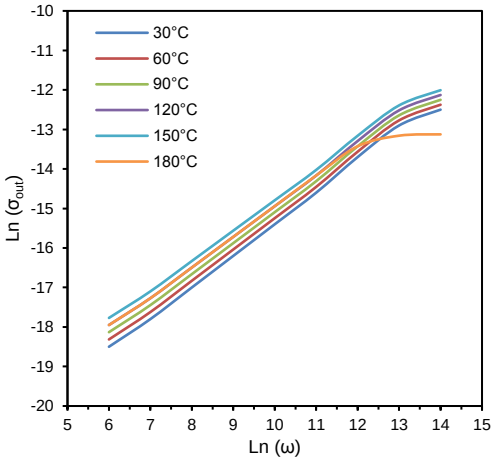

(c)

Fig. (2) Variation of $Ln(\sigma_{tot})$ with $Ln(\omega)$ for as-deposited $CuInGaS_2$ thin films and annealed at different temperatures for substrate temperature of (a) 20°C, (b) 100°C, and (c) 150°C

As shown in table (1), the exponent S, which is the slope of $dLn[\sigma_{tot}(\omega)]/d(\omega)$ decreases with increasing substrate temperature (T_S) in the low temperature range, while s increases at elevated temperatures, i.e., 150 °C, with increasing of T_S. The value of s increased with increasing heat treatment temperature of films deposited at T_S=100 °C. Also, s showed progress decreasing with oven temperature for samples deposited at 150 °C.

The AC activation energy, E_{AC}, for $CuInGaS_2$ films are estimated from the drawing of $Ln\sigma_{tot}(\omega)$ against the reciprocal absolute temperature, as indicated in Fig. (3).

Table (1) Values of s, τ and α for $CuInGaS_2$ thin films

T (°C)	As-deposited		
	S	τ x10^{-4} (s)	α
30	0.5853	-	0.1120
60	0.6395	-	0.1456
90	0.7131	-	0.1008
120	0.7971	-	0.1232
		0.398	0.0784
150	0.8341	-	0.0560
		0.159	0.1120
180	0.7911	-	0.1232
			0.1120

T (°C)	T_S=373K		
	S	τ x10^{-4} (s)	α
30	0.5348	-	0.3920
			0.1792
60	0.5444	13.281	0.1904
			0.1008
90	0.5089	13.281	0.1008
			0.1680
120	0.4638	-	0.2352
150	0.6219	-	0.0672
		0.796	0.0336
180	0.7911	-	0.1680
		0.159	0.1680

T (°C)	T_S=423K		
	S	τ x10^{-4} (s)	α
30	0.9567	-	0.2016
		0.0398	0.2800
60	0.9291	-	0.2240
		0.0398	0.2016
90	0.9039	13.281	0.1456
		0.0398	0.2800
120	0.8634	-	-
		0.0398	
150	0.8451	-	0.2240
		0.0398	0.1680
180	0.8152	-	0.2240
		0.0796	0.2016

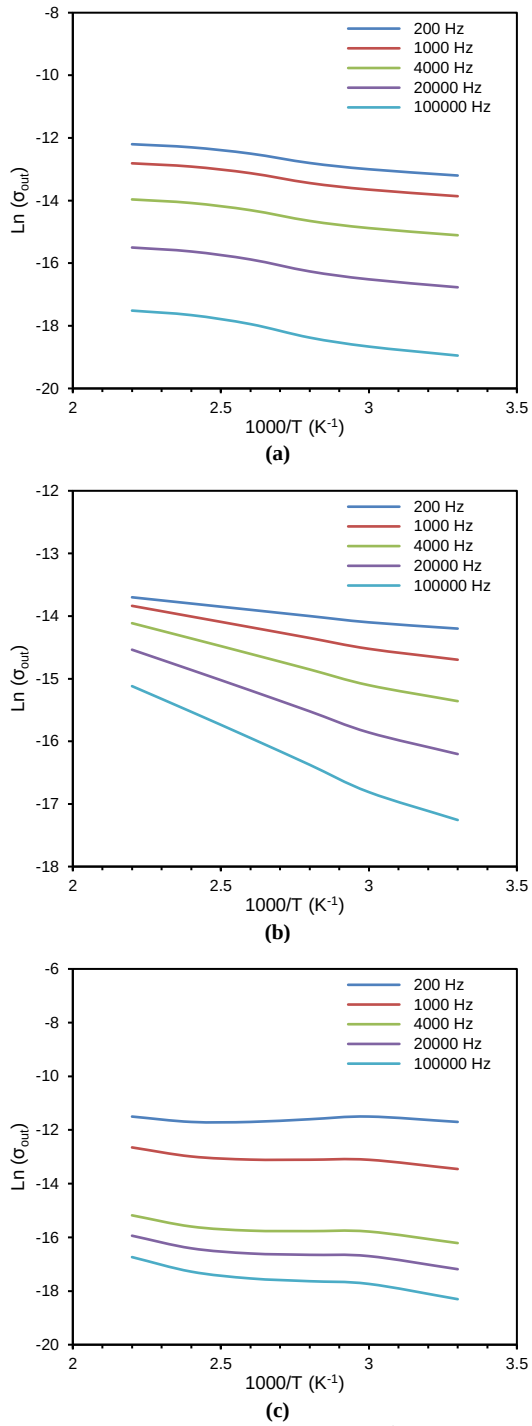

Fig. (3) Variation of Ln(σ_{tot}) with 1000/T for $CuInGaS_2$ thin films deposited at different substrate temperatures for substrate temperature of (a) 20°C, (b) 100°C, and (c) 150°C

Table (2) illustrates the E_{AC} values at selected frequencies (200 Hz, 1 kHz, 4 kHz, 10 kHz and 100 kHz). The results show that each sample declared one E_{AC}. On the other side, there is a direct relation between E_{AC} and frequency, while there is an inverse relation between E_{AC} and T_S. The E_{AC} decreases from 0.1132 to 0.0962 eV, while it increases from 0.1132 to 0.1258 eV with increasing frequency from 1 kHz to 100 kHz as well as increasing substrate temperature from 20 to 150 °C, respectively. The increase in frequency results in an increase of vibrating energy and hence the E_{AC} values will be decreased. This indicated that conductivity is purely AC, while the elimination of the localized states and vacancies explained the increase of E_{AC} with increasing T_S. The presence of large amount of trapping states at the grain boundary was proposed that able to capture free charge carries [31]. These charged states at grain boundary create potential barriers, which oppose the passage of carriers from grain to neighboring ones, where their sites increase with increasing T_S, which resulted in decreasing conductivity or increasing E_{AC} values.

Table (2) Values of E_{AC} for $CuInGaS_2$ thin films

Frequency (Hz)	E_{AC} (eV)		
	T_S (°C)		
	20	100	150
200	0.1132	0.1210	0.1258
1000	0.1115	0.1126	0.0517
4000	0.1022	0.1089	0.0336
10000	0.0973	0.0449	0.021
100000	0.0962	0.0103	0.0114

The real dielectric constant (ε_r) of $CuInGaS_2$ films prepared at different T_s, are measured within the employed frequency range (100Hz – 10MHz) as shown in Fig. (4). It is clearly from the ε_r pattern versus Log(ω), in Fig. (4) that the ε_r exhibits to increase with increasing heat treatment temperature, while it decreases with increasing frequency. This is ascribed to the fact that the electrode blocking layer is dominated, thus, the dielectric behavior is affected by the electrode polarization, while ε_r attained minimum values at high frequencies, which indicates that the dielectric signal is not affected by electrode polarization [8]. On the other hand, it is noticeable remarked that the values of ε_r, at frequency of 10^2 Hz, increase with increasing heat treatment and substrate temperatures. Indeed, the ε_r increases from 615 to 1064 and from 615 to 802 when heat treatment temperature increases from 30 to 180 °C and substrate temperature increases from 30 to 150 °C, respectively.

4. Conclusions

From the results obtained from this work, it can be concluded that the single phase with chalcopyrite structure of $CuInGaS_2$ becomes more pronounces at elevated temperatures. Also, similar variation sequence declared by α and τ values with the increment of substrate and treatment temperatures. The increase of α and τ refer to reduction of intermolecular force, while reducing of α and τ refers to the rising of intermolecular force. It is evident from the polarizability values that $CuInGaS_2$ thin films can be used as resistor in electronic circuits.

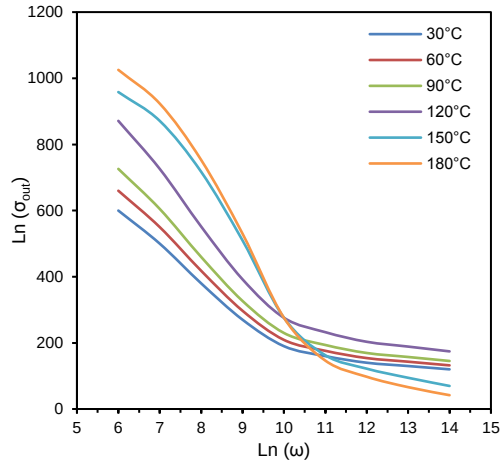

(a)

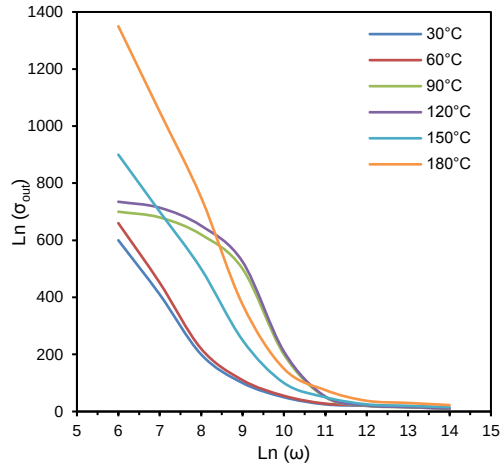

(b)

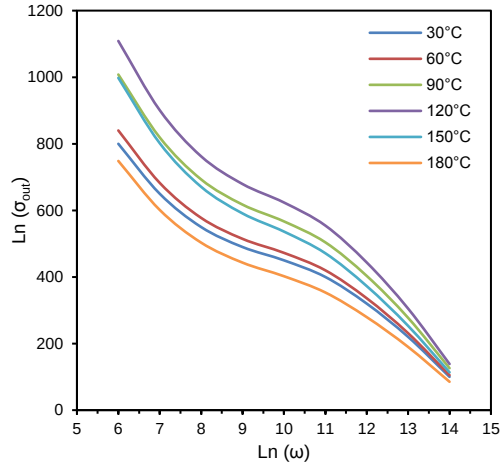

(c)

Fig. (3) Variation of ε_r with Lnω for as-deposited $CuInGaS_2$ thin films and annealed at different temperatures for substrate temperature of (a) 20°C, (b) 100°C, and (c) 150°C

References

[1] B.A. Hasan and D.A. Umran, "Dielectric permittivity and ac conductivity of CuInSeTe thin films", Semicond. Sci. Technol. 27 (2012) 125014.

[2] O.A. Hamadi, R.A. Markub and A.A.K. Hadi, "Heat-annealed enhanced-diffusion of silver in gallium arsenide", J Edu. Al-Mustansiriya Univ., 3 (2001) 35-44.

[3] B.A. Hasan, "AC Conductivity and dielectric analysis of CuInSSe Thin Films", Int. J. Thin Film Sci. Tech., 2(1) (2013) 29-36.

[4] O.A. Hamadi, K.Z. Yahiya and O.N.S. Jassim, "Properties of Silicon Carbide Thin Films Deposited by Vacuum Thermal Evaporation", J. of Semicond. Technol. Sci., 5(3) (2005) 182-186.

[5] R. Diaz, M. Leon and F. Reuda, "Characterization of Cu–In–Se–Te system in thin films grown by thermal evaporation," J. Vac. Sci. Technol. A, 10 (1992) 295-300.

[6] O.A. Hamadi and K.Z. Yahiya, "Optical and electrical properties of selenium-antimony heterojunction formed on silicon substrate", Sharjah Univ. J. Pure Appl. Sci., 4(2) (2007) 1-11.

[7] K. Inakoshi et al., "Preparation of $CuIn(S_xSe_{1-x})_2$ thin films by sulfurization and Selenization", Solar Energy Mater. Solar Cells, 50(1) (1998) 37-42.

[8] B.A.M. Badr, O.A. Hamadi and A.K. Yousif, "Measurement of thermooptic coefficient of semiconductors by single-beam scanning technique", Eng. Technol. J., 27(5) (2007).

[9] K. Subbaramiah and V. Sundara Raja, "Structural and optical properties of spray-deposited $CuIn(S_{1-x}Se_x)_2$ thin films", Thin Solid Films, 208 (1992) 247-251.

[10] O.A. Hamadi, "Characteristics of CdO-Si Heterostructure Produced by Plasma-Induced Bonding Technique", Proc. IMechE, Part L, J. Mater.: Design & Appl., 222 (2008) 65-71.

[11] T. Ohashi et al., "$CuIn(S_xSe_{1-x})_2$ Thin Films by Sulfurization", Jap. J. Appl. Phys., 34 (1995) 4159-4166.

[12] O.A. Hamadi, "Effect of Annealing on the Electrical Characteristics of CdO-Si Heterostructure Produced by Plasma-Induced Bonding Technique", Iraqi J. Appl. Phys., 4(3) (2008) 34-37.

[13] S. Kuranouchi and T. Nakazawa, "Study of one-step electrodeposition condition for preparation of $CuIn(Se,S)_2$ thin films", Solar Energy Mater. Solar Cells, 50 (1998) 31-36.

[14] A.A.K. Hadi and O.A. Hamadi, "Optoelectronic Characteristics of As-doped Si Photodetectors Produced by LID Technique", Iraqi J. Appl. Phys. Lett., 1(2) (2008) 23-26.

[15] L.I. Soliman and T.A. Hendia, "Influence of γ-irradiation on the optical and electrical properties of $ZnIn_2Se_4$ films", Rad. Phys. Chem., 50(2), 1997, 175-177.

[16] O.A. Hamadi, N.J. Shakir and F.H. Hussain, "Magnetic Field and Temperature Dependent Measurements of Hall Coefficient in Thermal Evaporated Tin-Doped Cadmium Oxide Thin Films", Bulg. J. Phys., 37(4) (2010) 223-231.

[17] L. Soliman, T. Hendlia and H. Zayed, "Effect of annealing on the switching properties of CuInSeTe thin films", Fizika A (Zagreb), 16(1) (2007) 39-46.

[18] O.A. Hamadi, "Profiling of Antimony Diffusivity in Silicon Substrates using Laser-Induced Diffusion Technique", Iraqi J. Appl. Phys. Lett., 3(1) (2010) 23-26.
[19] C. Landry, J. Lockwood and R. Barron, "Synthesis of Chalcopyrite Semiconductors and Their Solid Solutions by Microwave Irradiation", Chem. Mater. 7(4) (1995) 699-706.
[20] O.A. Hammadi and M.S. Edan, "Temperature Dependencies of Refractive Index and Optical Elasticity Coefficient on Lens Induced in Nd:YAG Crystal", Iraqi J. Appl. Phys., 8(1) (2012) 35-41.
[21] J.Y.W. Seto, "Deposition of Polycrystalline Silicon by Pyrolysis of Silane in Argon", J. Electrochem. Soc., 122(5) (1975) 701-706.
[22] O.A. Hammadi, "Photovoltaic Properties of Thermally-Grown Selenium-Doped Silicon Photodiodes for Infrared Detection Applications", Phot. Sen., 5(2) (2015) 152-158.
[23] S. Kumar et al., "Growth and Characterization of Copper, Indium and Copper- Indium Alloy Films non-aqueous Method of Electro Deposition", Indian J. Pure Appl. Phys., 46 (2008) 198-203.
[24] O.A. Hammadi and N.E. Naji, "Electrical and spectral characterization of CdS/Si heterojunction prepared by plasma-induced bonding", Opt. Quantum Electron., 48(8) (2016) 375-381.
[25] A.K. Jonscher, "Review Article: Dielectric relaxation in solids", J. Phys. D: Appl. Phys., 32(14) (1999) R57-R70.
[26] O.A. Hammadi, "Characteristics of Heat-Annealed Silicon Homojunction Infrared Photodetector Fabricated by Plasma-Assisted Technique", Phot. Sen., 6(4) (2016) 345-350.
[27] Z. Ahmad, **"Polymeric Dielectric Materials"**, Ch. 1 (2014) p. 4, doi: 10.5772/50638.
[28] O.A. Hamadi, "Characterization of SiC/Si Heterojunction Fabricated by Plasma-Induced Growth of Nanostructured Silicon Carbide Layer on Silicon Surface", Iraqi J. Appl. Phys., 12(2) (2016) 9-13.
[29] R. Bari and L. Patil, "Chemically Deposited n-$CuInSe_2$/Polyiodide Based PEC Solar Cells", Sensors and Transducers, 125 (2011) 213-219.
[30] O.A. Hammadi, "Synthesis and Characterization of Polycrystalline Carbon Nitride Nanoparticles by Fast Glow Discharge-Induced Reaction of Methane and Ammonia", Adv. Sci. Eng. Med., 11(5) (2019) 346-350.
[31] S. Sze and K. Kwok, **"Physics of Semiconductor Devices"**, 3rd ed., John Wiley & Sons, Inc. (NJ, 2007).

IRAQI JOURNAL OF APPLIED PHYSICS
Vol. 18, No. 1, January-February 2022, pp. 15-20

Sameer K. Hameed
Naseer A. Razzak
Abbas F. Mahood
Kareem L. Nahi

Department of Physics,
College of Science,
University of Thi Qar,
Nasiriyah, IRAQ

Optical Emission Spectroscopy of Laser-Produced Plasmas of Some Metal Targets

In this work, emission lines of laser-produced plasmas from three different metallic targets (copper, titanium and nickel) were detected by the optical emission spectroscopy. These plasmas were generated by irradiation of the metallic target with laser pulses of high peak power in room environment. Both electron density and electron temperature were determined for the three targets at different peak laser powers using the ratios of line intensities based on the obtained emission spectra. Electron temperatures were determined in the range 0.34-0.442 eV for copper target at laser power of 70 MW, 0.281-0.418 eV for titanium target at laser power of 60 MW, and 0.35-0.46 eV for nickel target at laser power of 70 MW.

Keywords: Laser-produced plasma; Emission line; Electron density; Electron temperature
Received: 02 January 2022; **Revised:** 29 January 2022; **Accepted:** 05 February 2022

1. Introduction

Pulsed-laser induced plasma of solids is the subject of investigation in many fields of applied research such as laser plasma sources to x-ray lasers, inertial confinement fusion and laboratory astrophysics [1-3]. A pulsed laser source is employed to vaporize and excite the analyte forming plasma [4]. The optical emission from the relaxation of excited species within the plasma yields information regarding the composition of the material under test [5-7]. The plasma and its characteristics (electron density, electron temperature, spatial and temporal behavior) depend on the target's thermophysical properties and laser beam parameters, such as laser pulse, temporal duration and shape, laser wavelength and energy [8-12]. Plasma descriptions start by trying to characterize the properties of the assembly of atoms, molecules, electrons and ions rather than the individual species [13]. If thermodynamic equilibrium exists, the plasma properties such as the description of the speed of the particles and the relative populations of energy level can be described through the concept of the temperature [14-17].

The electron temperature is an equally important plasma parameter which can be spectroscopically determined in a variety of ways: from the ratio of integrated line intensities, from the ratio of line intensity to underlying continuum and from the shape of the continuum spectrum [18-21]. The diagnostic techniques employed for the determination of electron density includes plasma spectroscopy, Langmiur probe, microwave and laser interferometry and Thomson scattering [22-24]. Spectroscopy technique is the simplest as far as instrumentation is concerned [25].

Laser-induced breakdown spectroscopy (LIBS) is a rapid chemical analysis technology that uses a short laser pulse to create a micro-plasma on the sample surface [26-28]. This analytical technique offers many compelling advantages compared to other elemental analysis techniques [29]. These include a sample preparation-free measurement experience, extremely fast measurement time (usually a few seconds) for a single spot analysis, broad elemental coverage, including lighter elements, such as H, Be, Li, C, N, O, Na, and Mg, versatile sampling protocols that include fast raster of the sample surface and depth profiling, and finally thin-sample analysis without the worry of the substrate interference [30-34]. A typical detection limit of LIBS for heavy metallic elements is in the low-ppm range [35]. LIBS is applicable to a wide range of sample matrices that include metals, semiconductors, glasses, biological tissues, insulators, plastics, soils, plants, soils, thin-paint coating, and electronic materials [36].

For LIBS, Echelle spectrographs are typically used. For analysis of a wide range of samples, a system based on an Echelle spectrograph offers a combination of high resolution and wide wavelength coverage [37]. It is also possible to relay the laser light to the sample and collect the signal by fiber optics. The gating requirements of LIBS are not very demanding [38]. Gate times and delays of several microseconds are typical. The intensity of the plasma emission is usually high enough to allow good spectra to be recorded in single scan mode [39].

In this work, emission lines of laser-produced plasmas from three different metallic targets (copper, titanium and nickel) are detected by the optical emission spectroscopy. These plasmas are generated by irradiation of the metallic target with Nd:YAG laser pulses of high peak power in room environment. Both electron density and electron temperature are determined for the three targets at different peak laser powers using the ratios of line intensities based on the obtained emission spectra.

2. Experiment

The optical emission spectra of copper, titanium and nickel plasmas were recorded using the experimental setup of laser-induced breakdown spectroscopy (LIBS) shown in Fig. (1). It consists of pulsed Nd:YAG laser of 1064 nm wavelength, 9 ns duration, 1 Hz pulse repetition frequency and peak power up to 120 MW. The laser beam was focused on the surface of the irradiated sample located at the focal length of a converging lens (f=10cm). An optical fiber holding photodetector was adjusted at 45° with beam direction at 5 cm distance from the sample where plasma is generated. The emission from the tin plasma plume was recorded using Ocean Optics HR 4000 CG-UV-NIR spectrum analyzer in the spectral range 320-750 nm.

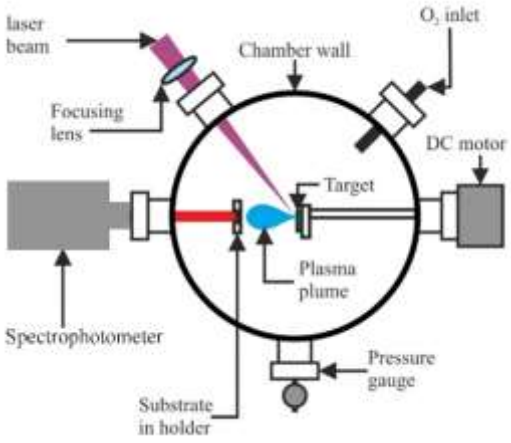

Fig. (1) The experimental setup for the laser-induced breakdown spectroscopy used in this work

3. Results and Discussion

The optical emission spectra of laser-produced plasmas of copper, titanium and nickel in the range 300-800 nm are shown in Fig. (2). The prominent spectral lines of copper target in room environment (Fig. 2a) are Cu I (421.2 nm), Cu II (642.5 nm) and Cu III (713.1 nm) in addition to other lines with low intensities those will be neglected when determining both electron density and electron temperature. Similarly, the prominent spectral lines of titanium target in room environment (Fig. 2b) are Ti I (414.3 nm), Ti II (635.6 nm) and Ti III (706.2 nm) in addition to other lines with low intensities those will be neglected too when determining both electron density and electron temperature. For nickel target, the prominent spectral lines in room environment (Fig. 2c) are Ni I (407.4 nm), Ni II (628.7 nm) and Ni III (699.3 nm) in addition to other lines with low intensities those will also be neglected when determining both electron density and electron temperature. The transitions are identified using the spectral database of National Institute of Standards and Technology (NIST) [21].

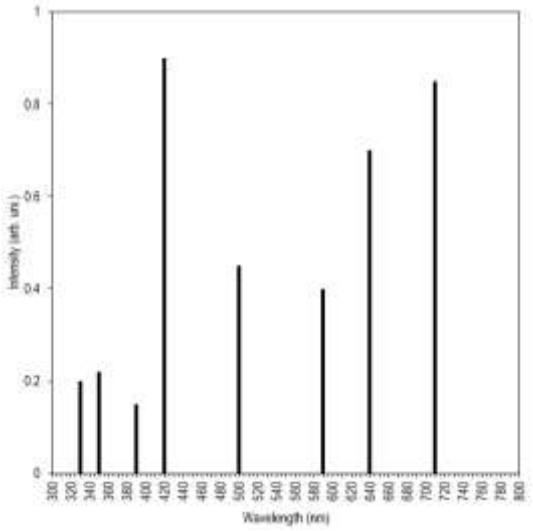

(a)

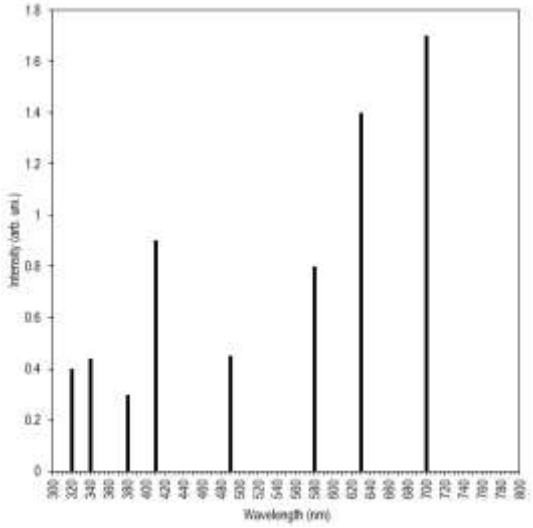

(b)

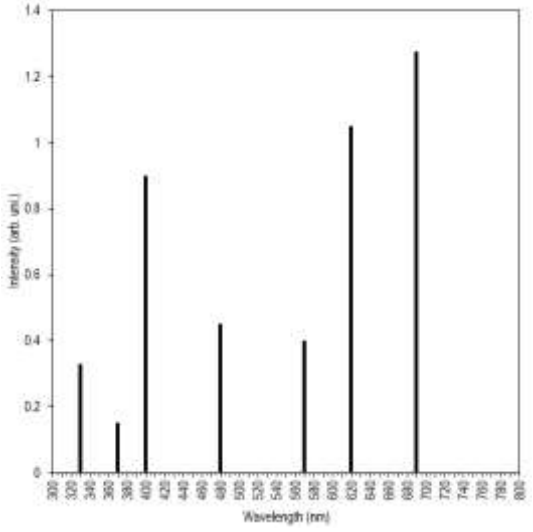

(c)

Fig. (2) Optical emission spectra of (a) copper, (b) titanium and (c) nickel plasmas produced by pulsed laser of 55 MW peak power

The intensities of copper plasma lines at 421.2, 642.5 and 713.1 nm were measured at different laser

peak powers. Figure (3a) shows the influence of the laser peak power on the spectral line intensities. In similar manner, the intensities of titanium plasma lines at 414.3, 635.6 and 706.2 nm as well as the intensities of nickel plasma lines at 407.4, 628.7 and 699.3 nm were also measured at different laser peak powers, as in Fig. (3b) and (3c).

As shown, the emission intensity of the spectral lines increases with increasing laser peak power from 20 to 120 MW. This is due to the absorption of laser photon by the plasma and the plasma transparency to the laser beam. Therefore, the ablation of the metallic target increases [22]. Such increase produces a consequent increase in the height and emission of produced. At higher values of laser peak powers, plasma shielding effect is observed, i.e., the plasma becomes opaque to the laser beam which shields the target so the lines intensities decreases.

A major difference between the variations of line intensity with laser power for the three metallic targets can be seen in the full-width half maximum (FWHM). The emission spectra for copper target are reasonably narrower than those of titanium target. The FWHM for Cu III line is 48 nm while the FWHM for Ti III is 600 nm. For nickel target, the spectra are apparently wide enough to consider the determination of the FWHM. The highest intensities of the Ti III (706.2 nm) and Ni III (699.3 nm) are noticeably comparable but lower than that of Cu III (713.1 nm).

One of the important parameters for using optical spectroscopy for isotopic analysis is linewidth to line separation. Optical transitions, both atomic and molecular, are not immune to environmental factors and hence never provide precisely sharp line structures. While LA is a powerful technique for generating ions, atoms, and molecules from a solid material, the species are generated in a high-temperature and high-electron density environment. These conditions lead to significant spectral line broadening, which may reduce the ability to resolve small isotope splittings. Prominent broadening mechanisms that influence spectral linewidths in a laser-produced plasma are Doppler, pressure, and Stark effects. An in-depth knowledge of these line broadening mechanisms in a laser-produced plasma system is ultimately important to employ optical spectroscopy for isotopic analysis.

On the other hand, the intensities of nickel target lines at higher laser powers (>80 MW) are higher than those of copper and titanium at the same values of laser powers. These differences are related to the physical and chemical properties of these metals as the surface and environmental conditions are sufficiently kept the same.

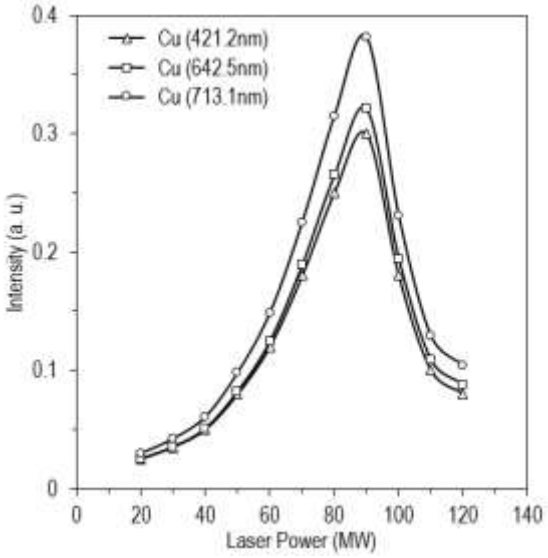

(a)

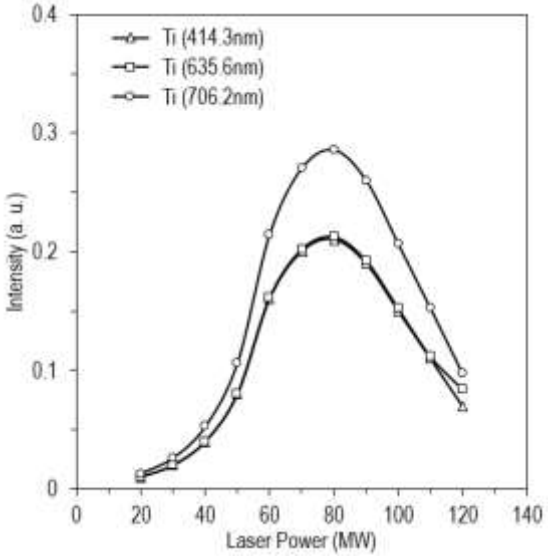

(b)

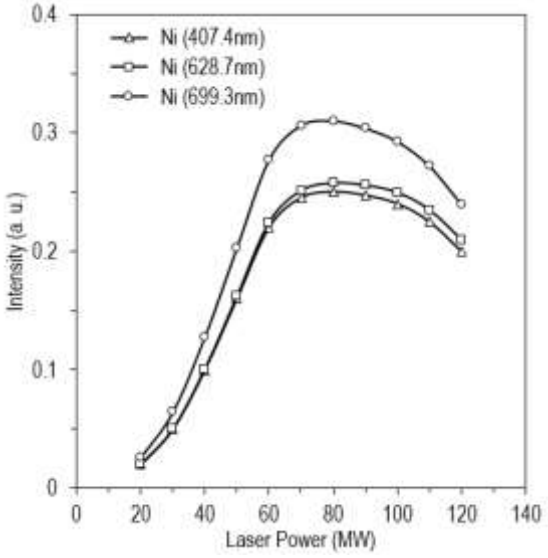

(c)

Fig. (3) Variation of emission intensity with laser peak power for the three metallic targets used in this work (a) copper, (b) titanium and (c) nickel

Under the assumption that the plasma in local thermodynamic equilibrium (LTE), the lower limit of the electron density is given by [23]:

$$n_e \geq 1.6 \times 10^{12} (\Delta E)^3 (T_e)^{\frac{1}{2}} \quad (1)$$

where n_e is the electron density, T_e is the electron temperature and ΔE is the energy difference between the states. The values of n_e are obtained from Saha-Boltzmann equation as [14]:

$$n_e = \frac{2(2\pi m_e k_B T_e)^{3/2}}{h^3} \frac{I^I_{mn} A_{ij} g^{II}_i}{I^{II}_{ij} A_{mn} g^I_m} e^{-\frac{E_{ion}+E^{II}_i-E^I_m}{k_B T_e}} \quad (2)$$

where m_e is the electron mass, k_B is Boltzmann constant, h is Planck's constant and E_{ion} is the ionization potential of the neutral species in its ground state, I_{ji} is the intensity of the spectral line of the transition from level j to i, λ_{ji} is the wavelength, A_{ji} is the transition probability, g_j is the statistical weight, E_j is the energy value of higher level

Figure (4) shows the electron density of laser-induced plasmas of copper, titanium and nickel at different laser peak powers. It can be observed that for all the metallic targets, the electron density grows as the laser peak power is increased. The reason is that when a solid sample is irradiated by Nd:YAG laser pulses, a collision-induced process occurs and hence free electrons in the focal volume are accelerated by the electric field of the laser beam and gained energy by colliding with neutral atoms. When the electrons have gained amount of energy, they can ionize atoms by collision and this causes the electron density to grow with the laser peak power. The electron density dramatically decreases at high laser peak powers, this is due the plasma shielding as discussed previously.

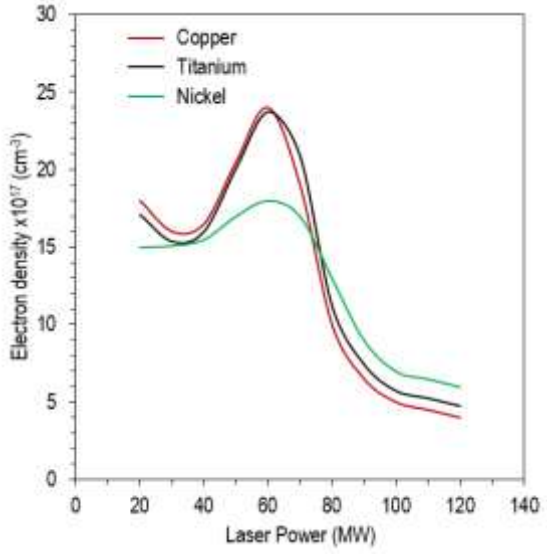

Fig. (4) Variation of electron density of laser-induced plasmas generated in this work with laser peak power

The electron temperature (T_e) can be calculated using the ratio of two lines of the same species of the ionization stage as [23]:

$$T_e = \frac{\Delta E}{k_B \ln\left(\frac{\lambda_2 I_2 g_1 A_1}{\lambda_1 I_1 g_2 A_2}\right)} \quad (3)$$

where I, λ, g, A , and E are the total intensity, wavelength, statistical weight, absorption oscillator strength and excitation energy of one of the lines, respectively. Primed quantities are those for the second line. These values for the two lines considered are taken from tables of the National Institute of Standards and Technology (NIST) [14]

The electron temperatures for the three metallic targets were calculated using Eq. (3) from the ratios of the intensities of emission lines. Figure (5) shows that the electron temperature (T_e) increases with increasing laser peak power. The electron temperature is strongly dependent on the laser peak power as the latter is the source of evaporation, atomization and ionization of the target when focused on.

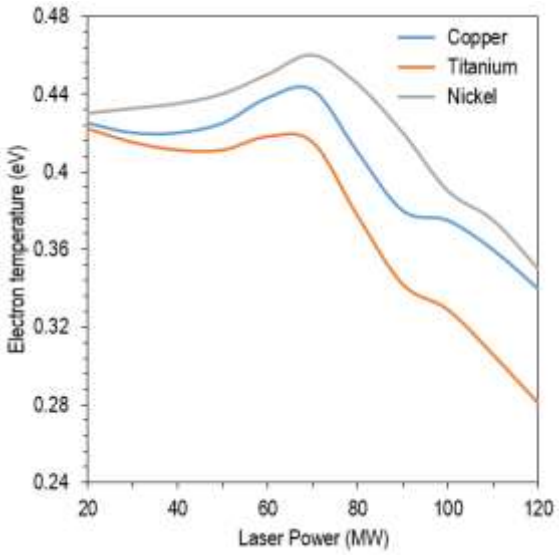

Fig. (5) Variation of electron temperature of laser-induced plasmas generated in this work with laser peak power

4. Conclusion

Three different metallic targets (copper, titanium and nickel) were irradiated by Q-switched Nd:YAG laser pulses to produce transient and elongated plasmas. Measurements of electron density and temperature were carried out by optical emission spectroscopy technique. Line intensity ratios of the successive ionization stages of the metal target were used for the determination of electron temperature and Stark broadened profile of first ionized tin species was used for the electron density measurements. The dependencies of electron density and electron temperature on different experimental parameters like distance from the target surface were studied. The electron temperatures in the range of 0.34-0.442 eV, 0.281-0.418 eV and 0.35-0.46 eV were obtained for the copper, titanium and nickel plasmas, respectively, while electron densities down to 4x1017 cm^{-3} and up to 23.76x1017 cm^{-3} were observed.

References

[1] S. Palmer and K. Leroy, "Pulsed-laser induced

plasma of ionic solids", Appl. Phys. Rep., 14(1) (2000) 39-48.
[2] A.K. Yousif and O.A. Hamadi, "Plasma-induced etching of silicon surfaces," Bulg. J. Phys., 35(3), 191–197, 2008.
[3] R.A. Ismail et al., "Full characterization at 904nm of large area Si p-n junction photodetectors produced by laser-induced diffusion," Int. J. Mod. Phys., 19(31), 197–201, 2007.
[4] O.A. Hammadi and N.E. Naji, "Electrical and spectral characterization of CdS/Si heterojunction prepared by plasma-induced bonding," Opt. Quantum Electron., 48(8), 1–7, 2016. DOI 10.1007/s11082-016-0647-2
[5] R.A.H. Hassan and F.T. Ibrahim, "Preparation and Characterization of Anatase Titanium Dioxide Nanostructures as Smart and Self-Cleaned Surfaces", Iraqi J. Appl. Phys., 16(4) (2020) 13-18.
[6] M.A. Hameed and Z.M. Jabbar, "Preparation and Characterization of Silicon Dioxide Nanostructures by DC Reactive Closed-Field Unbalanced Magnetron Sputtering", Iraqi J. Appl. Phys., 12(4) (2016) 13-18.
[7] E.A. Al-Oubidy and F.J. Al-Maliki, "Photocatalytic activity of anatase titanium dioxide nanostructures prepared by reactive magnetron sputtering technique", Opt. Quantum Electron., 51(1) (2019) 23.
[8] O.A. Hamadi, "Profiling of Antimony Diffusivity in Silicon Substrates using Laser-Induced Diffusion Technique", Iraqi J. Appl. Phys. Lett., 3(1) (2010) 23-26.
[9] T. Dominguez et al., "Optical emission of excited states in laser-produced plasma", Sci. Eng. Rev., 8(6) (2002) 101-112.
[10] S.H. Faisal and M.A. Hameed, "Heterojunction Solar Cell Based on Highly-Pure Nanopowders Prepared by DC Reactive Magnetron Sputtering", Iraqi J. Appl. Phys., 16(3) (2020) 27-32.
[11] F.J. Kadhim and A.A. Anber, "Highly-Pure Nanostructured Silicon Nitride Films Prepared by Reactive DC Magnetron Sputtering", J. Indust. Eng. Sci., 25(5) (2016) 91-94.
[12] M. Arab et al., "Comparison Study of Two Commercial Spectrometers for Heavy Metal Analysis of Laser Induced Breakdown Spectroscopy (LIBS)", Phot. Sens., 4(1) (2014) 63-69.
[13] O.A. Hammadi, M.K. Khalaf and F.J. Kadhim, "Fabrication and characterization of UV photodetectors based on silicon nitride nanostructures prepared by magnetron sputtering," Proc. IMechE Part N: J. Nanoeng. Nanosys., 230(1), 32–36, 2015. DOI: 10.1177/1740349915610600.
[14] J. Keen and D. Monahan, **"Emission Spectroscopy of Laser-Produced Plasmas in Atmospheric Environment"**, Dollhouse Publishing (NY, 2004), 145, 233, 381.
[15] K.S. Khashan and O.A. Hamadi, "Features of spot-matrix surface hardening of low-carbon steel using pulsed laser", Eng. Technol. J., 25(2) (2007).
[16] M.A. Hameed, S.H. Faisal, R.H. Turki, "Characterization of Multilayer Highly-Pure Metal Oxide Structures Prepared by DC Reactive Magnetron Sputtering Technique", Iraqi J. Appl. Phys., 16(4) (2020) 25-30
[17] D.A. Cremers and L. J. Radziemski, **"Handbook of Laser-Induced Breakdown Spectroscopy"**, John-Wiley & Sons, Ltd. (Chichester, 2006).
[18] R.A.H. Hassan and F.T. Ibrahim, "Preparation and Characterization of Ni-doped TiO_2 Nanostructures for Surface Cleaning Applications", Iraqi J. Appl. Phys., 17(1) (2021) 3-8.
[19] O.A. Hamadi and K.Z. Yahiya, "Optical and electrical properties of selenium-antimony heterojunction formed on silicon substrate", Sharjah Univ. J. Pure Appl. Sci., 4(2) (2007) 1-11.
[20] S. Ben Zakour and H. Taleb, "Shift Endpoint Trace Selection Algorithm and Wavelet Analysis to Detect the Endpoint Using Optical Emission Spectroscopy", Phot. Sens., 6(2) (2016) 158-168.
[21] O.A. Hamadi, "Characteristics of CdO-Si Heterostructure Produced by Plasma-Induced Bonding Technique", Proc. IMechE, Part L, J. Mater.: Design & Appl., 222 (2008) 65-71.
[22] F.J. Al-Maliki and E.A. Al-Oubidy, "Effect of gas mixing ratio on structural characteristics of titanium dioxide nanostructures synthesized by DC reactive magnetron sputtering", Physica B: Cond. Matter, 555 (2019) 18-20
[23] A.K. Sharma et al., "Diagnostic technique for determination of ion and electron parameters using plasma spectroscopy", App. Phot. Spect., 9(1) (2014) 69-78.
[24] O.A. Hamadi, "Characterization of SiC/Si Heterojunction Fabricated by Plasma-Induced Growth of Nanostructured Silicon Carbide Layer on Silicon Surface", Iraqi J. Appl. Phys., 12(2) (2016) 9-13.
[25] C. Perez et al., "Detection limit of LIBS for low-ppm heavy metallic elements", Chem. Anal. Appl., 12(8) (2018) 1045-1054.
[26] O.A. Hamadi, B.A.M. Bader and A.K. Yousif, "Electrical Characteristics of Silicon p-n Junction Solar Cells Produced by Plasma-Assisted Matrix Etching Technique", Eng. Technol. J., 28 (2008).
[27] D. Zhong and Z. Li, "Material Measurement Method Based on Femtosecond Laser Plasma Shock Wave", Phot. Sens., 7(1) (2017) 1-10.
[28] O.A. Hamadi, "Effect of Annealing on the

Electrical Characteristics of CdO-Si Heterostructure Produced by Plasma-Induced Bonding Technique", Iraqi J. Appl. Phys., 4(3) (2008) 34-37.

[29] H. R. Griem, **"Plasma Spectroscopy"**, McGraw-Hill (NY, 1964).

[30] O.A. Hammadi, M.K. Khalaf and F.J. Kadhim, "Fabrication of UV photodetector from nickel oxide nanoparticles deposited on silicon substrate by closed-field unbalanced dual magnetron sputtering techniques," Opt. Quantum Electron., 47(2), 1–9, 2015. DOI: 10.1007/s11082-015-0247-6

[31] R.H. Turki and M.A. Hameed, "Spectral and Electrical Characteristics of Nanostructured NiO/TiO_2 Heterojunction Fabricated by DC Reactive Magnetron Sputtering", Iraqi J. Appl. Phys., 16(3) (2020) 39-42.

[32] O.A. Hammadi, "Photovoltaic properties of thermally-grown selenium-doped silicon photodiodes for infrared detection applications," Phot. Sens., 5(2), 152–158, 2015. DOI: 10.1007/s13320-015-0241-4

[33] W.L. Wiese and G.A. Martin, "Wavelengths and Transition Probabilities for Atoms and Atomic Ions", Part II, National Bureau of Standards, Washington, DC, (1980).

[34] O.A. Hammadi and M.S. Edan, "Temperature Dependencies of Refractive Index and Optical Elasticity Coefficient on Lens Induced in Nd:YAG Crystal", Iraqi J. Appl. Phys., 8(1) (2012) 35-41.

[35] M.V. Allmen and A. Blatter, **"Laser-Beam Interaction with Materials: Physical Principles and Applications"**, Springer-Verlag, Berlin, 2nd ed., (1995).

[36] F.J. Al-Maliki, O.A. Hammadi and E.A. Al-Oubidy, "Optimization of Rutile/Anatase Ratio in Titanium Dioxide Nanostructures prepared by DC Magnetron Sputtering Technique", Iraqi J. Sci., 60(special issue) (2019) 91-98.

[37] A.W. Miziolek, V. Palleschi and I. Schechter, **"Laser-induced breakdown spectroscopy: fundamentals and applications"**, Cambridge University Press, 2006.

[38] O.A. Hammadi, "Fabrication of High-Quality Microchannels for Biomedical Applications Using Third-Harmonic Radiation of Nd:YAG Laser", J. Laser Sci. Eng., 10(2) (2018) 61-64.

[39] K. Song, Y., L. Lee and J. Sneddon, "Applications of laser induced breakdown spectrometry," Appl. Spect. Rev., 32(3) (1997) 183-235.

IRAQI JOURNAL OF APPLIED PHYSICS
Vol. 18, No. 1, January-March 2022, pp. 21-26

Characterization of CdSe/Si Heterostructures Synthesized by Plasma-Induced Bonding Technique

Oday A. Hamadi [1]
Noor E. Naji [2]

[1] *Department of Physics, College of Education, Al-Iraqia University, Baghdad, IRAQ*
[2] *School of Applied Sciences, University of Technology, Baghdad, IRAQ*

In this work, the characteristics of the CdSe-Si structure produced by plasma-induced bonding technique were studied. The produced structure was an asymmetric heterojunction consisting of n-type CdSe on a p-type silicon substrate. The Si substrate and CdSe sample were bonded by subjecting them to the plasma formed between two electrodes. The measurements included the structural and electrical characteristics. The built-in potential of the produced heterojunction is about 0.9 eV with typical spectral responsivity within the range 300-900 nm. With dark current of 1 μA, maximum forward current of 136 μA and ideality factor lower than unity, the results explained better characteristics than those of the same heterojunction produced by thermal evaporation technique.

Keywords: Heterojunction; Plasma-induced bonding; Electronic transport; Semiconductors
Received: 18 January 2022; Revised: 24 February 2022; Accepted: 3 March 2022

1. Introduction

Direct bonding means the joining of two smooth and clean surfaces at room temperature. No constraint on lattice matching exists and after joining the two surfaces, the bonded pairs are annealed at a high temperature to ensure the formation of strong bonding. With proper procedure the bonded interface can achieve bulk strength.

Although the main driving force for development of bonding has been production of silicon-on-insulator (SOI), several other high potential applications of bonding have emerged in microelectromechanical systems (MEMS) and as a way of integrating dissimilar crystalline materials. To reach a sufficient level of maturity, bonding procedures need to be optimized and standardized according to the application. Also, bonding requires a high-temperature annealing step after the room temperature joining, to ensure the formation of a strong and uniform bonding. This high temperature annealing is sometimes incompatible with many applications and it may cause material degradation, especially when bonding thermally mismatched materials. Back to the pioneering days, low temperature bonding procedures have been highly desirable.

If two solids with clean and flat surfaces are brought into close proximity at room temperature, attractive forces pulls the two bodies together into intimate contact so that bonds can form across the interface. The phenomenon was given rather little attention until in the last decades when semiconductors bonding found several applications in mirco-mechanics, microelectronics and optoelectronics.

There are many factors governing the bonding behavior of two surfaces. First, the surfaces must be flat and smooth. Usually it is argued that surfaces can make contact only at some asperities. However, the success of bonding technique has followed the development of modern semiconductor chemical-mechanical polishing (CMP) technology. The semiconductor polishing technology has reached such a level of maturity that, nowadays, commercial silicon wafers have surface roughness in the order of 10^{-10}m. The second parameter governing the ability for bonding is the surface chemical state and surface termination. For most semiconductors, surface preparation and cleaning techniques are well-developed and characterized. However, in silicon technology the surface chemical treatments are more standardized and established processes, as compared to, for example, compound semiconductors.

The basic procedure in semiconductor bonding technique starts with mirror-polished surfaces that are cleaned, plasma-activated and given their final surface termination using a combination of chemical treatments. The wafers are then brought together at room temperature and if proper surface conditions apply, the solids will bond spontaneous. After room temperature bonding, a heat treatment at elevated temperature is performed to strengthen the interface bonding. Typical bonding technique procedures are fully compatible with microelectronic process technologies, offering several advantages both in available processing equipment and possible applications.

One of the great potentials of the bonding approach is the integration of dissimilar materials. Integration of dissimilar semiconductor by hetero-epitaxial growth is hampered by the difference in

lattice constants. Particularly, combining III-V compounds semiconductors with highly developed silicon circuits has been pursued in recent years with the goal to incorporate photonic and high-speed devices with advanced silicon technology [1-2].

A problem that sometimes occurs in the bonding technique is the presence of interface bubbles or voids. Macroscopic voids appear at the bonded interface due to trapped particles or dust contamination, surface protrusion and trapped gas. To avoid contamination of particles and dust on the surface before bonding, the bonding technique is preferably performed in a clean-room environment, or in a micro clean-room set-up [3]. Particles inhibit interaction between the opposing surfaces, and as a consequence a 1μm dust particle trapped at the interface commonly results in an unbounded area (void) of 1cm in diameter. Ionic contamination represents another category of contaminants. These contaminants mainly affect the electrical properties of the bonded interface. Especially boron from the clean-room environment has been proposed as a coarse contamination in the bonding technique. Boron contamination of the surfaces before bonding results in a p-doped layer near the bonded interface after annealing [4].

When the solids have been bonded together at room temperature usually the interaction, or bonding energy, is relatively weak. Therefore, a heat treatment is performed to increase the bond-strength. The annealing enhances out-diffusion of interface trapped molecules and desorption of chemisorbed surface atoms, such as hydrogen. At the same time the annealing activates formation of covalent bonds between the bonded surfaces, like solid-to-solid bonding in the case of hydrophobic bonding. The thermal treatment used to increase the bond-strength can, unfortunately, also cause severe problems in bonding technique. For instance, when bonding dissimilar materials, the thermal mismatch induced high stresses in the material. High temperature annealing also restricts the use of metal patterns and can cause diffusion of dopants.

Generally, the bonding requires a high-temperature annealing step to ensure the formation of strong bonding between solids, i.e. to form covalent bonds. In silicon-to-silicon bonding usually an annealing above 1000°C is required, and in bonding involving compound semiconductors, the annealing is usually performed above 600°C. Such a high-temperature annealing is incompatible with many applications. Particularly, pre-structured wafers that already contain temperature-sensitive structures cannot be exposed to the high-temperature annealing. The high-temperature annealing also induces material degradation. It can cause broadening of diffusion layers. When bonding dissimilar materials, annealing at high temperatures would induce large thermal stress due to the difference in thermal expansion coefficients [5-10].

Chemically reactive plasma discharges are widely used to modify the surface properties. The relative importance of a specific discharge depends on input power, gases, reactor volume and geometry, gas flows, etc. For instance, plasma discharges are employed for etching, deposition or surface cleaning. The gas-chemistry and the plasma parameters (effect, applied voltage, pressure, plasma density, etc.) that are being used govern the plasma/surface interactions. A variety of gases are such as Ar, O_2, SF_6, Cl_2 and CHF_3 are used for this purpose.

The plasma affects a surface mainly in two ways: physically and chemically. Physical plasma/surface interaction is due to bombardment of energetic ions. The bombarding ions cause sputtering, mixing and defect formation. Chemical interaction is driven by chemically active species in the plasma. Plasma is a partially ionized gas with equal number of positive and negative charges. At steady state, the free electrons acquire sufficient energy from the applied electric field to produce impact ionization of the gas, at a rate equal to the loss rate. Since the electrons are more mobile due to their lower masses, they diffuse faster to the surrounding surfaces, including substrate surface and chamber wall. This builds up a negative potential at the surrounding surfaces, while the plasma is 'depleted' from negative charges. Therefore, the plasma potential is always positive. As a result, the electric field between the positively charged plasma and the negatively charged surroundings, induce an ion current, which is equal to the electron diffusion current at equilibrium. A body immersed into plasma hence acquires a negative floating potential. The ions in the plasma are accelerated through the plasma sheath and bombard the surrounding surfaces. However, by applying an external field, the energy of the ions bombarding the substrate can be adjusted. Many capacitive discharges are asymmetric, because the RF-driven electrode area is smaller than the grounded area, which is usually the chamber wall. This causes the driven electrode to acquire a self-bias DC offset voltage.

The freedom to integrate diverse materials is one of the advantageous features of the bonding technique. In design, no consideration has to be taken to use lattice-matched materials. Several high-potential applications are reported using dissimilar materials integration by bonding. As mentioned above, a commercial success was achieved with wafer bonded LED. A low-dark-current 20GHz photodetector using an InGaAs absorption layer and a Si avalanche multiplication layer have been demonstrated [11]. Others have solved the problem of poor quality mirrors in VCSEL's by wafer fusing high-reflecting mirrors to the active region [12]. Fabrication of semiconductor lasers directly on Si substrates have also been achieved using wafer bonding [13].

In this work, a CdSe/Si heterojunctions were fabricated by plasma-induced bonding technique and their electrical and spectroscopic characteristics were determined and analyzed.

2. Experimental Work

A (100)-oriented p-type silicon wafer of 500 μm thickness and 3 Ω.cm resistivity was used in this work. Also, high purity (0.9999) cadmium selenide (CdSe) was used to form 250 μm-thick samples. Both samples, Si and CdSe, were washed with distilled water then rinsed in ethanol and subjected to ultrasonic waves for 10 minutes, then dried by hot air. The silicon samples were then cleaned with HF for 5 minutes to remove any residual oxides which have existed on their surfaces. Both samples were softly grinded and polished to obtain flat surfaces. Then, these samples were rinsed in ethanol to remove acids then dried to be ready for processing.

The Si and CdSe samples were mounted inside a homemade plasma chamber that was initially evacuated down to 10-3 mtorr using a double-stage rotary pump then to 10^{-5} mtorr using a diffusion pump. The silicon substrate was mounted on a holder made of stainless steel at a specified distance from the anode and the CdSe sample was placed on the Si substrate. The samples were placed at a position that the plasma is entirely surrounding the sample. Discharge voltage and current are 15 kV_{DC} and 3 A, respectively. Argon gas at a pressure of (1 mtorr) was used to generate the discharge plasma. The sample was maintained inside the operated system for 10 minutes before being removed and tested.

Before bonding, the native oxide is removed from the surfaces to have a solid-to-solid bonding [14-15]. However, the bonding is very weak at room temperature and after low-temperature annealing because of the hydrogen-terminated surface. A high-temperature annealing above 500 °C is necessary to desorb hydrogen from surface and enable a covalent bonding.

The difference in thermal expansion between CdSe and Si will induce high mechanical stress in the material when annealing the bonded samples at high-temperatures. The thermal stress degrades the material by generating defects. It can also cause cracks and completely debond. The main degradation occurs in CdSe since Si is a mechanically stronger material.

Electrical measurements were carried out using a Farnel DC power supply and Keithley-616 digital electrometer while the C-V measurements were performed using *hp*/4192 ALF LCZ device. The samples were subjected heating up to 600 °C within 5 minutes then left to return to its initial temperature within the same period of time. Topography of the treated samples was performed using Leitz-Metallux optical microscope at different magnifications (50x, 100x, 150x).

In this work, eight CdSe/Si samples were prepared to introduce the repeatability of this technique. Along eight days, a sample was daily prepared and processed at the same conditions. As will be shown later, the presented results are the average of the best five samples those seemed identical to each other. Therefore, this technique has very good repeatability as the preparation and processing conditions are kept stable as possible. The experimental preparation and processing conditions mentioned above can be considered as the optimum to obtain the best results in this work. These results were compared to the data available in the literature as well as the results obtained by several local works.

3. Results and Discussion

If two identical solids with the same orientation are bonded together without misalignment and without interface contamination, they should merge into one. However, there are always deviations from the ideal case. In the bonding technique, there is always an unavoidable misalignment between the bonded solids and therefore misfit dislocations appear. Misfit dislocations will also appear at the bonded interface if two solids of different orientation or different lattices are bonded. The presence of native oxides, adsorbed surface contaminants and interface bubbles (voids), also inhibit a perfect solid-to-solid transition region. Figure (1) explains the structure of the bonded samples where the misfit in the CdSe-Si interface is shown.

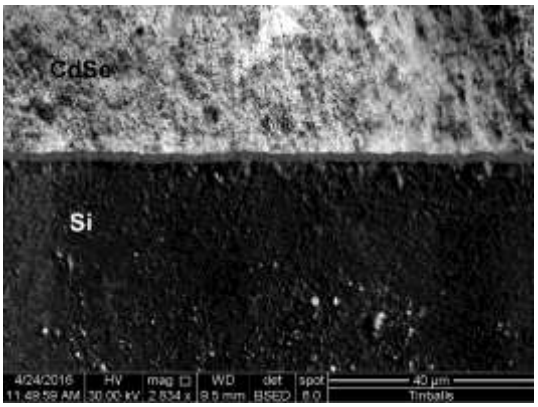

Fig. (1) The SEM image of the CdSe-Si interface

Defect-etching techniques were found to be more suited for investigations of bulk material defect introduced by the bonding technique, arising mainly from thermal mismatch stress. Defect-etching uses etch selectivity to reveal crystal imperfection such as dislocation. The dislocation appears as pits on CdSe surface and their origin is traced from the shape of the pits, as shown in Fig. (1). For Si and other semiconductors, defect-etching techniques are well developed and frequently used.

A generalized theory for bonding technique may be difficult to achieve since the electrical properties of the bonded interface depends on many parameters.

The electrical properties vary between different reports and it is likely that such deviations are linked to variations in bonding procedures. Care has to be taken in properly removing contaminants, metallic and organic, from the surfaces before bonding. The disordered interface being composed of misfit dislocation acts as gettering and segregation site in the same way as grain boundaries in polycrystalline semiconductors. Misalignment between the solids has been reported to increase junction resistance due to electrical charging of misfit dislocation. When bonding compound semiconductors, crystallographic aligning of the bonded wafers to an angle below 4° reduced the junction resistance, irrespectively of the lattice mismatch between the wafers [16].

Wafer bonded p-n heterojunction characteristics are heavily affected by the non-ideal interface. However, a substantial improvement of wafer bonded p-n heterojunctions characteristics is usually obtained by shifting the p-n transition away from the bonded interface, either by high temperature annealing [17-18] or by implantation [19-20]. Alternatively, the p-n heterojunction formed under UHV conditions and low temperatures results in an ideality factor no more than 1.18 and indicates low recombination at the interface. Bonding p-n heterojunction in ambient air and subsequent high temperature annealing was seen to yield high recombination near the bonded interface. An ideality factor lower than 1 was obtained and low minority carrier lifetime [21]. Figure (2) shows the I-V characteristics of bonded p-n Si-CdSe heterojunction. As shown, the dark current is about 1 μA and the forward current is uniformly linear. The illumination current in the reverse biasing reaches a maximum of about 136 μA. The bonded interface is often avoided in the electrically active region of the electronic device. However, the recombination centers of the defective bonded interface are used to control the minority carrier lifetime in power devices. These characteristics are typically enhanced compared to results obtained by another techniques such as thermal evaporation, sputtering and chemical bath deposition [22-24].

In order to introduce the nature of the anisotype CdSe-Si heterojunction, the C-V measurements were performed in the reverse biasing and results are presented in Fig. (3). The built-in potential was determined for the CdSe-Si heterojunction to be about 0.9 V.

The spectral responsivity of the CdSe-Si heterojunction was determined as a function of wavelength as shown in Fig. (4). This heterojunction responds in the 400-750 nm range much more than in the range below 400 nm. The maximum spectral responsivity of 0.62 A/W was recorded at 540 nm. This cheap technique presents an advantage to produce good photodetectors for the wavelengths longer than 400 nm.

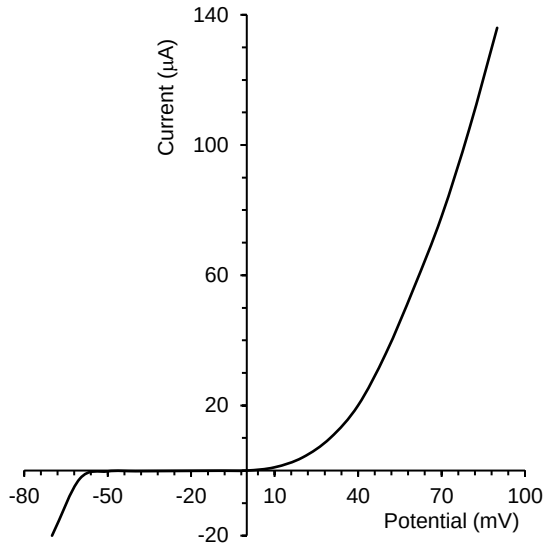

Fig. (2) The I-V characteristics of the CdSe-Si heterojunction fabricated in this work

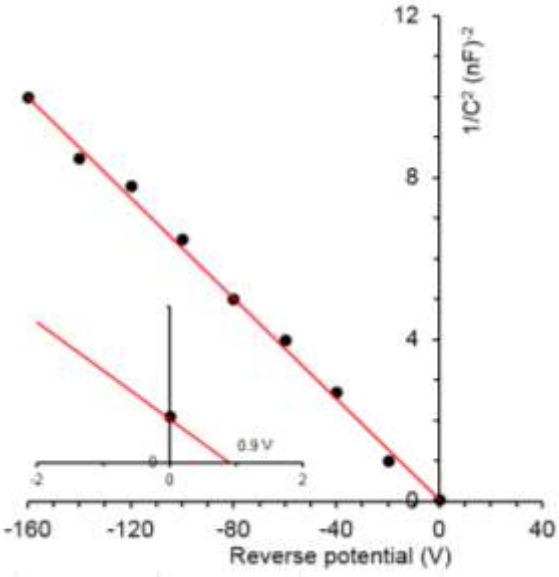

Fig. (3) The C-V characteristics of the CdSe-Si heterojunction fabricated in this work under reverse bias potential

Integration of CdSe and Si has attracted much interest since the unique properties in each material can be combined in devices or systems, such as CdSe-based piezoelectric devices and optoelectronics components.

The epitaxial growth of CdSe on Si substrate is hampered by the difference between the lattice constants of the materials. However, using bonding for the integration, the lattice-mismatch becomes no obstacle. Unfortunately, there is a large difference in thermal expansion between CdSe and Si. When bonding solids of dissimilar materials and annealing at elevated temperatures, the thermal mismatch will induce high thermal stress in the material.

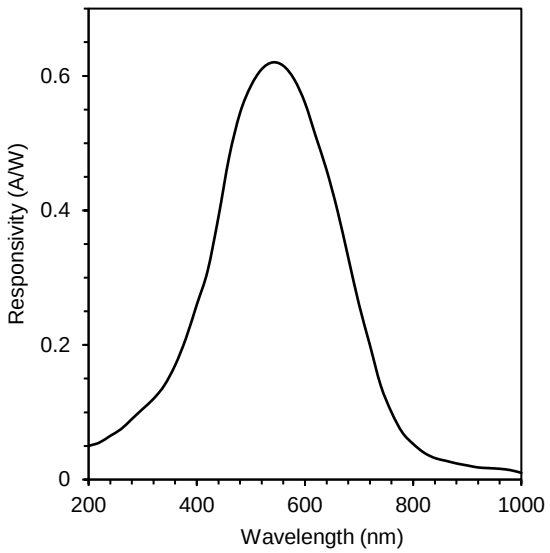

Fig. (4) The spectral responsivity of the CdSe-Si heterojunction fabricated in this work

In each material system, nature has imposed a set of physical properties, such as mobility, optical absorption, electrical resistivity, thermal and mechanical properties. For a given application, the optimal properties may not reside in a single material but in a variety of dissimilar materials. A specific case is to combine compound semiconductor that have direct band gap and high mobility with Si that is extensively used in microelectronic applications.

For lattice-matched materials systems, the material integration is extensively and routinely realized using hetero-epitaxy. However, for material systems that are largely lattice-mismatched, hetero-epitaxial growth has not been able to produce the high quality material needed in optoelectronics [25-27]. Hetero-epitaxial growth of CdSe on Si has been a subject of interest and although improvement is continuing, the densities of threading dislocations in CdSe seem to have saturated at more than ten thousand times higher than the value for lattice-matched epitaxy on CdSe. The dislocation density at the interface of hetero-epitaxial grown CdSe/Si junction is found to be around $10^{10}cm^{-2}$. The dislocation density and material quality have been improved by indirect growth of CdSe on Si using SiO_2 intermediate buffer layers or various epitaxial layer overgrowth (ELO) and conventional growth techniques. The principal feature in ELO is that growth proceeds laterally over a cap-layer, which inhibits transmission of threading dislocation [28].

4. Conclusions

A CdSe-Si heterojunction was produced by plasma-induced bonding techniques. The structural characteristics explained the good bonding interface between the CdSe and Si samples. Electrical measurements showed reasonable enhancement in the heterojunction characteristics compared to that produced by another techniques. Despite the complexity imposed by the plasma processing system, production of heterojunctions with such enhanced characteristics has advantages of low cost and large size devices.

References

[1] Y. Zhou, A. H. Zhu, Y.-H. Lo, C. Ji, S. A. Bashar, A. A. Allerman, T. Hargett, R. Sieg, K. D. Choquette, "Oxide-defined GaAs vertical cavity surface-emitting lasers on Si substrates, *IEEE Photon. Lett.* 12, p. 110, (2000)

[2] D. L. Mathine, The integration of III-V optoelectronics with silicon circuitry, *IEEE J. Selec. Top. Quantum Electron.*, 3, p. 952, (1997).

[3] R. Stengl, K.-Y- Ahn and U. Gösele, Bubble-Free Silicon Wafer Bonding in a Non-Cleanroom Environment, *Jpn. J. Appl. Phys.* 27, L2364 (1988).

[4] F. P. Widdershoven, J. Haisma, J. Naus, Boron contamination and antimony segregation at the interface of directly bonded silicon wafers, *J. Appl. Phys.* 68, p. 6253, (1990).

[5] U. Gösele, J. Steinnkirchner, T. Martini, M. Reiche, G. Kästner, Silicon wafer bonding via designed monolayers, *Adv. Mater.*, 7 (7), pp. 662-665 (1995).

[6] H. Takagi, K. Kikuchi, R. Maeda, T.R. Chung, T. Suga, Surface activated bonding of silicon wafers at room temperature, *Appl. Phys. Lett.* 68, p. 2222, (1996).

[7] U. Gösele, H. Stenzel, T. Martini, J. Steinkirchner, D. Conrad, K. Scheerschmidt, Self-propagating room-temperature silicon wafer bonding in ultrahigh Vacuum, *Appl. Phys. Lett.*, 67, p. 3614, (1995).

[8] A. Berthold, B. Jakoby, M. J. Vellekoop, Wafer-to-wafer fusion bonding of oxidized silicon to silicon at low temperatures, *Sensors & Actuators*, A68, p. 410, (1998).

[9] Q.-Y. Tong, W. J. Kim, T.-H. Lee, U. Gösele, Low Vacuum Wafer Bonding, *Electrochem. Solid State Lett.* 1, p. 52, (1998).

[10] G. Krauter, A. Schumacher, U. Gösele, T. Jaworek, G. Wagner, Room Temperature Silicon Wafer Bonding with Ultra-Thin Polymer Films, *Adv. Mater.*, 9, p. 417, (1997).

[11] B. Levine, C. J. Pinzone, S. Hui, C. A. King, R. E. Leibenguth, D. R. Zolnowski, D. V. Lang, H. W. Krautter, M. Geva, Ultralow-dark-current wafer-bonded Si/InGaAs photodetectors, *Appl. Phys. Lett.* 75, p. 2141 (1999).

[12] A. Black, A. R. Hawkins, N. M. Margalit, D. I. Babic, A. L. Holmes, Y.-L. Chang, P. Abraham, J. E. Bowers, E. L. Hu., Wafer fusion: materials issues and device results**,** *IEEE J. Select. Topics Quantum Electron.* 3 , p. 943 (1997).

[13] H. Wada, H. Sasaki and T. Kamijoh, Wafer bonding technology for optoelectronic integrated

devices, *Solid Stat. Electron.* 43, p. 1655, (1999).
[14] D. Kikuchi, S. C. Adachi, Chemically cleaned InP(100) surfaces in aqueous HF solutions, *Mater. Sci. Eng.* ***B***, 76, p. 133, (2000).
[15] L. A. Zazzera, J. F. Moulder, XPS and SIMS Study of Anhydrous HF and UV/Ozone-Modified Silicon (100) Surfaces, *J. Electrochem. Soc.*, 136, p. 484, (1989).
[16] F. A. Kish, D. A. Vanderwater, M. J. Peansky, M. J. Ludowise, S. G. Hummel, S. J. Rosner, Low-resistance ohmic conduction across compound semi-conductor wafer-bonded interfaces, *Appl. Phys. Lett*., 67, p. 260, (1995).
[17] U. Gösele, H. Stenzel, T. Martini, J. Steinkirchner, D. Conrad, and K. Scheerschmidt, Self-propagating room-temperature silicon wafer bonding in ultrahigh vacuum, *Appl. Phys. Lett.* 67 (24), pp. 3614-3616 (1995).
[18] P. Kopperschmidt, G. Kästner, D. Hesse, N. D. Zakharov and U. Gösele, High bond energy and thermomechanical stress in silicon on sapphire wafer bonding, *Appl. Phys. Lett.* 70 (22), pp. 2972-2974 (1997).
[19] A. Hawkins, W. Wu, P. Abraham, K. Streubel, J. E. Bowers, High Gain-Bandwidth-Product Silicon Heterointerface Photodetector, *Appl. Phys. Lett.*, 70, p. 303, (1996).
[20] H. Yamaguchi, S. Fujino, T. Hattori, Y. A. Hamakawa, Superjunction by Wafer Direct Bonding, *Jpn. J. Appl. Phys.* 34, p. L199 (1995).
[21] D. Pasquariello and K. Hjort, Mesa-Spacers: enabling non-destructive measurements of surface energy in room temperature wafer bonding, *J. Electrochem. Soc.*, 147, pp. 2343-2346 (2000)
[22] M. Ashry and S. Fares, "Electrical Characteristic Measurement of the Fabricated CdSe / P-Si Heterojunction Solar Cell under Radiation Effect", *Microelectron. Solid State Electron.*, 1(2) (2012) 41-46.
[23] W.N. Ibrahim, "Optoelectronic Properties of CdSe/Si Heterojunction", *Eng. Technol. J.*, 30(12) (2012) 2138-2149.
[24] Santhosh T.C.M., Kasturi V. Bangera., G.K. Shivakumar., "Preparation of vacuum deposited cadmium selenide thin films for optoelectronic applications", *Mater. Today Proc.*, 3 (2016) 2220-2224.
[25] A. Fontcuberta i Morral, J.M. Zahler and H.A. Atwater, InGaAs/InP double heterostructures on InP/Si templates fabricated by wafer bonding and hydrogen-induced exfoliation, *Appl. Phys. Lett.* 83 (26), pp. 5413-5415 (2003).
[26] M. Sugo, Y. Takanashi, M. M. Al-Jassim, M. Yamaguchi, Heteroepitaxial growth and characterization of InP on Si substrates, *J. Appl. Phys.* 68, 2, p. 540-547, (1990).
[27] H. Itakura, T. Suzuki, Z.K. Jiang, T. Soga, T. Jimbo and M. Umeno, Effect of InGaAs/InP strained layer superlattice in InP-on-Si, *J. Cryst. Growth*, 115, p.154-157, (1991).
[28] D. S. Wuu, R. H. Horng, M. K. Lee, Indium phosphide on silicon heteroepitaxy: Lattice deformation and strain relaxation, *J. Appl. Phys.* 68, 7, pp. 3338, (1990).

IRAQI JOURNAL OF APPLIED PHYSICS
Vol. 18, No. 1, January-March 2022, pp. 27-30

Characteristics of Cu_2O-Doped Sn_2O_3 Nanostructures Deposited on Porous Silicon Substrates as Gas Sensors

Jitban N. Jasbijn
Tibibe J. Tibsibim
Govbe U. Jasbijn

Department of Technology of Materials Processing, Faculty of Geological Prospecting, Institute of Mining and Mining Technologies
Kyrgyz State Technical University, Urban, KYRGYZSTAN

In this work, nanostructured Sn_2O_3 thin films with different Cu_2O content (2-10 at.%) were prepared by pulsed-laser deposition (PLD) method. The film samples with 2, 4, 6, 8 and 10 at.% of Cu_2O showed Sn_2O_3 peaks of wurtzite structure. We have studied the operation temperature of gas sensors fabricated from the prepared samples at different etching times (5-60 min) and different environment temperatures (50-350°C) and found that the maximum sensitivity was about 79% for porous silicon prepared after etching time of 10 min.

Keywords: Gas sensor; Copper oxide; Tin oxide; Porous silicon
Received: 17 October 2021; **Revised:** 21 January 2022; **Accepted:** 28 January 2022

1. Introduction

The artificial olfaction system is a very promising tool to monitor the off-odors in the field. Usual odor measurement techniques use human olfaction or conventional analytical techniques [1,2]. The first category represents the real odor perception but is not applicable to measure continuously bad odors in the field. The second class of techniques provides the mixture composition, but not the global information representative of the odor perception. The e-nose has the potentiality to combine "the odor perception" and the "field monitoring". The instrument, based on non-specific gas chemical sensor arrays combined with a chemo-metric processing tool provides a suitable technique for in site monitoring of off-odors. The research group in Arlon has more than a decade of experience in the field measurement of environmental odors. Published studies report attractive results [3,4]. This technique has probably the best potentialities to answer to the expectations of the various actors of the environmental problems in relation with the odors annoyance [5]. However, a number of limitations are associated with the properties of chemical sensors [6,7], the signal processing performances and the real operating conditions of the environmental field [8]. The field experience of the research group has shown that the metal oxide based gas sensors are the best chemical sensors for long term application, more than one year of continuous work. However, as a result of harsh environmental conditions, hardware limitations and olfactory pollution specificities, real-time odor monitoring with the electronic nose is always a real challenge. The instrument has to cope with several specific drawbacks. In particular, it has to automatically compensate the time drift [9] and the influence of ambient parameters such as temperature or humidity [10]. This paper is focused on the time drift and the long term stability of the metal oxide gas sensors. Sensor drift is a first serious impairment of gas sensors. The sensors alter over time and therefore have poor repeatability, since they produce different responses for the same odor. That is particularly troublesome for electronic noses. The sensor signals can drift during the learning phase [11]. Another frequent problem encountered in the field and particularly in highly polluted atmosphere is the sensor failure or an irreversible sensor poisoning. Clearly, life expectancy of sensors is reduced in real-life operation when compared with clean lab operations. Sensor replacement is generally required to address such issue, but, after replacement, odors should still be recognized without having to recalibrate the whole system [12]. But commercial sensors are rarely reproducible. In order to appraise the time evolution of the sensors and the effect on the results of an electronic nose, experiments were performed during several years on two identical sensor arrays. The signals of two "identical" sensors array, placed in the same measurement chamber, were observed during several years. After a state of the art of the sensors drift correction techniques [13-20], the most relevant methods for the field has been tested and the results compared in order to select the best one for our application.

Metal oxide semiconductors have attracted significant attention in gas sensing applications due to their simple implementation, low cost, and good reliability for real-time control systems with respect to other gas sensors [21-28]. The gas sensing properties of metal oxide semiconductors are influenced by many factors such as their operating temperatures, morphology and chemical composition of the films [29]. In such gas sensors, the change in the electrical conductivity is due to the interaction of the targeted gas molecules (chemisorption or physisorption) with the surface of the metal oxide grains. Consequently, metal oxide sensors show changes in the resistance under exposure to oxidizing

or reducing gases. [24,30]. Since the majority of these sensitive layers are n-type, p-type semiconductors sensitive to gases are highly demanded for gas sensing applications such as sensor arrays for electronic nose [31].

These p-type semiconductor gas sensors have much different sensing pattern from their n-type counterparts [32]. In addition, it is also reported that p-type semiconductors are more appropriate for detecting oxidizing gases such as nitrogen dioxide [33]. At elevated temperatures, the presence of chemically adsorbed molecules such as nitrogen dioxide can cause electron depletion at the surface of the metal oxide grains; and consequently, the electrical resistivity of the thin films increases [22]. The competition between chemisorptions of nitrogen dioxide and atmospheric oxygen, at the same active surface sites of the metal oxide layer, plays an important role in determining the specific nitrogen dioxide/metal oxide interaction [34].

The diffusion of copper into Sn_2O_3 can cause the formation of complex centers (Cu_{Sn}, Cu_i). It is possible that copper atoms can replace either substitutional or interstitial Sn atoms in the Sn_2O_3 lattice creating structural deformations [35,36]. Copper oxide significantly affects the electrical, chemical, structural and optical properties of Sn_2O_3, and the study of the electronic state of Cu in Sn_2O_3 was the subject of interest for a long time [37-39].

2. Experiment

Tin oxide powder with different doping concentrations for Cu_2O at (2-10) at.% Cu_2O pressing it under 5 tons to form a target with 2.5 cm in diameter and 0.2 cm in thickness. It should be as dense and homogenous as possible to ensure good quality Cu_2O:Sn_2O_3 thin films deposited at different doping ratios (2, 4, 6, 8 and 10 at.%) by PLD technique, whose experiments are carried out inside a vacuum chamber that initially evacuated down to 10^{-3} torr. The focused Q-switched Nd:YAG laser beam is incident at angle of 45° on the target surface. The substrate is placed in front of the target with its surface parallel to that of the target. The film thickness was determined by a Spectroscopic Reflectometer SR300 and found to be 120 nm with a tolerance of ±7 nm.

Layers of porous silicon (PS) were prepared by electrochemical etching where the silicon wafer serves as the anode, as shown in Fig. (1), while the cathode is made of platinum. Both are immersed in $HF/H_2O_2/H_2O$ mixture of 1:1:1 mixing ratio as an electrolyte. A p-type silicon wafer was used as a starting substrate in the photochemical etching. The samples were cut from the wafer and rinsed with acetone and methanol to remove dirt, as well as to remove the native oxide layer on the samples. The electrochemical etching process was carried out at constant current 40 mA and different times (10, 25 and 60 min).

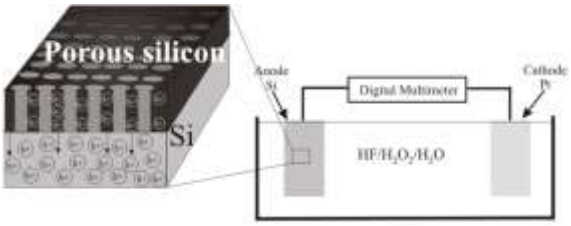

Fig. (1) Experimental setup to prepare porous silicon

3. Results and Discussion

Figure (2) shows the sensitivity for nitrogen dioxide gas with 10 ppm concentration, as a function of operation temperature in the range of 27-350 °C for Cu_2O:Sn_2O_3 (0.98-0.02) wt.% which are deposited on porous (111) Si wafers at different etching times. It can be seen from Fig. (2) that the sensitivity of all films increases with increasing operating temperature to reach a maximum value corresponding to an optimum operating temperature of 150 °C for all samples. Beyond this temperature, the sensitivity to nitrogen dioxide gas of all samples decreases at about 350 °C. The high temperature operation of the sensor makes the lifetime of the sensor shorter and increase its resistance, thus more electrical power is required for operation. It is believed that the oxygen could be removed or lost from the bulk of the metal oxide materials at high temperatures. This suggests that the response of the sensor may decrease at higher temperatures since there will be more oxygen vacancies, which lead to less occurrence of the reaction between nitrogen dioxide and oxygen.

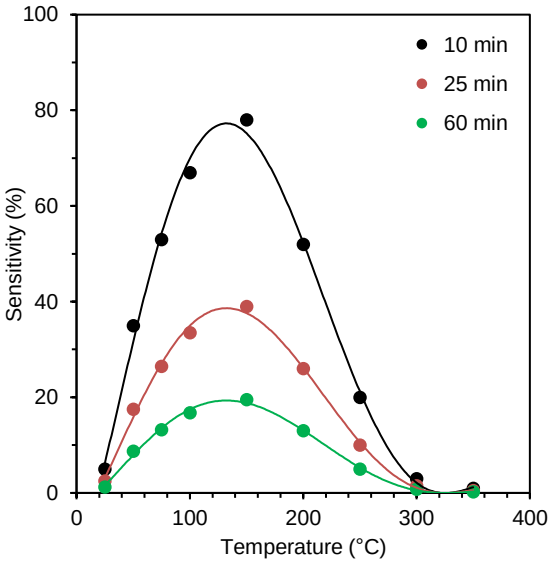

Fig. (2) Variation of sensitivity with operating temperature for different etching times on porous silicon

Decreasing etching time leads to increase the sensitivity of sensors to nitrogen dioxide gas and improve the sensor response at 200 °C. The sensing process depends on the surface roughness which increases detection sensitivity. The films prepared at

porous times of 10 min have higher values of sensitivity because the surface roughness is high.

Figure (3) shows the variation of response time with porous time at different operation temperatures. This figure reveals that the response time decreases with increasing porous current at operation temperatures lower than 200 °C, while the response time increases with increasing porous time from 10 to 60 min at higher operation temperature (>200°C).

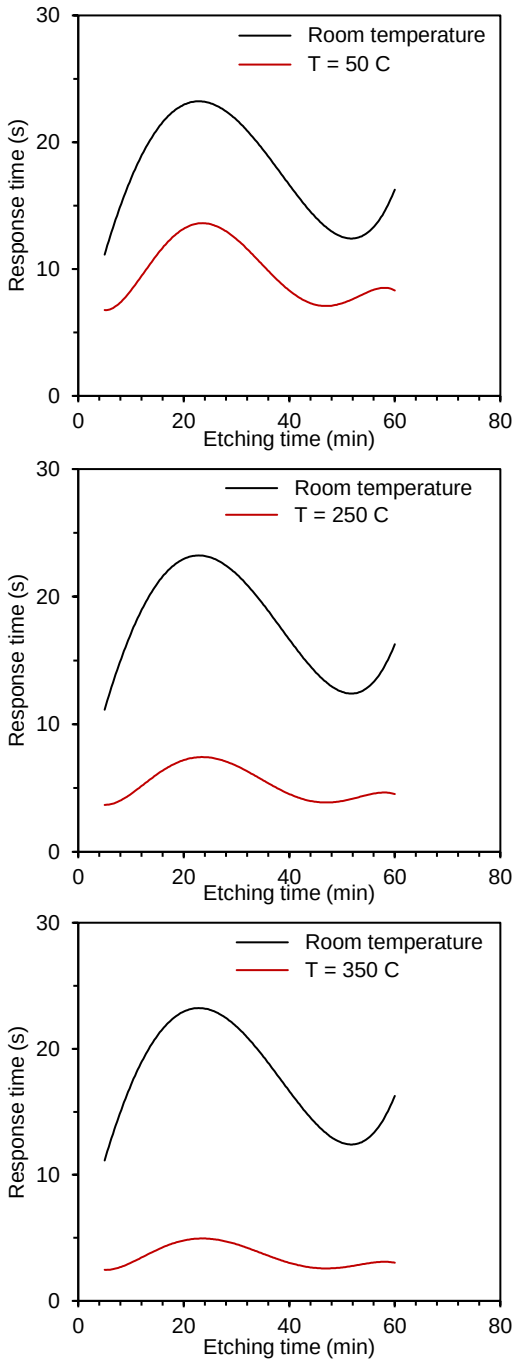

Fig. (3) Comparisons of response time variation with etching time at different operating temperatures with room temperature condition

The reduction in the grain size due to increasing porous time allows the space charge to cover large volume of the grain and the large number of grain boundaries provides large area for adsorption of O^- and O^{-2}. Hence, large variations in the barrier and resistance can enhance the reactivity at lower temperatures. Also, the density of surface states increases with the reduction in the particle size, or it can help in lowering the operation temperature.

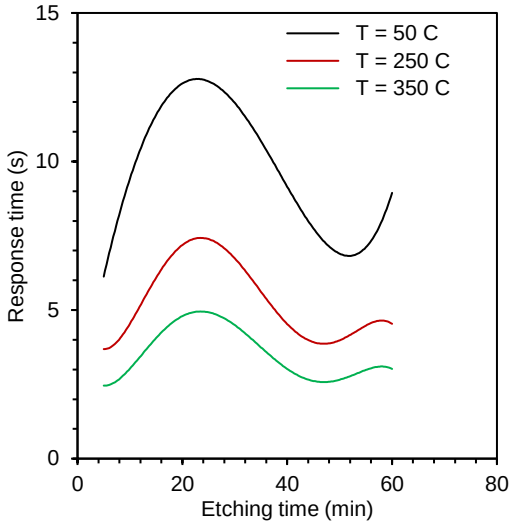

Fig. (4) Effect of operating temperature on variation of response time with etching time

4. Conclusions

In concluding remarks, polycrystalline Cu_2O-doped Sn_2O_3 structures were successfully prepared by PLD technique. We have studied the operation temperature of gas sensors fabricated from the prepared samples at different etching times (5-60 min) and different environment temperatures (50-350°C) and found that the maximum sensitivity was about 79% for porous silicon prepared after etching time of 10 min.

References

[1] A.C. Romain et al., "Odour annoyance assessments around landfill sites: methods and results", *NOSE 08 , Int. Conf. on Environ. Odour Monit. Control* Rome, 6-8 July, 2008.

[2] A.C. Romain et al., "Use of a simple tin oxide sensor array to identify five malodours collected in the field", *Sens. Actuat. B: Chem.*, 62(1) (2000) 73-79.

[3] W. Bourgeois et al., "The use of sensor arrays for environmental monitoring: interests and limitations", *J. Environ. Monit.*, 5(6) (2003) 852-860.

[4] O.A. Hamadi, B.A.M. Bader and A.K. Yousif, "Electrical Characteristics of Silicon p-n Junction Solar Cells Produced by Plasma-Assisted Matrix Etching Technique", Eng. Technol. J., 28 (2008).

[5] N. Barsan, D. Koziej and U. Weimar, "Metal oxide-based gas sensor research: How to?", *Sens. Actuat. B: Chem.*, 121(1) (2007) 18-35.

[6] C. Pijolat et al., "Tin dioxide gas sensor as a tool for atmospheric pollution monitoring: Problems and possibilities for improvements", *J. Mater. Sci.*, 38 (2003) 4333-4346.

[7] A.C. Romain, P. André and J. Nicolas, "Three years experiment with the same tin oxide sensor arrays for the identification of malodorous sources in the environment", *Sens. Actuat. B: Chem.*, 84(2-3) (2002) 271-277.
[8] O.A. Hamadi, "Profiling of Antimony Diffusivity in Silicon Substrates using Laser-Induced Diffusion Technique", Iraqi J. Appl. Phys. Lett., 3(1) (2010) 23-26.
[9] M. Holmberg et al., "Drift counteraction in odour recognition applications: Lifelong calibration method", *Sens. Actuat. B: Chem.*, 42(3) (1997) 185-194.
[10] O. Tomic et al., "Recalibration of a gas-sensor array system related to sensor replacement", *Anal. Chim. Acta*, 512(2) (2004) 199-206.
[11] O.A. Hammadi, "Photovoltaic Properties of Thermally-Grown Selenium-Doped Silicon Photodiodes for Infrared Detection Applications", Phot. Sen., 5(2) (2015) 152-158.
[12] M. Zuppa et al., "Drift counteraction with multiple self-organising maps for an electronic nose", *Sens. Actuat. B: Chem.*, 98 (2004) 305-317.
[13] R. Ionescu, A. Vancu and A. Tomescu, "Time-dependent humidity calibration for drift corrections in electronic noses equipped with SnO_2 gas sensors", *Sens. Actuat. B: Chem.*, 69(3) (2000) 283-286.
[14] O. Tomic, H. Ulmer and J.-E. Haugen, "Standardization methods for handling instrument related signal shift in gas-sensor array measurement data", *Anal. Chim. Acta*, 472(1-2) (2002) 99-111.
[15] C. Di Natale, A. Martinelli and A. D'amico, "Counteraction of environmental disturbances of electronic nose data by independent component analysis", *Sens. Actuat. B: Chem.*, 82(2-3) (2002) 158-165.
[16] O.A. Hammadi and N.E. Naji, "Electrical and spectral characterization of CdS/Si heterojunction prepared by plasma-induced bonding", Opt. Quantum Electron., 48(8) (2016) 375-381.
[17] J.-E. Haugen, O. Tomic and K. Kvaal, "A calibration method for handling the temporal drift of solid state gas-sensors", *Anal. Chim. Acta*, 407(1-2) (2000) 23-39.
[18] T. Artursson et al., "Drift correction for gas sensors using multivariate methods", J. Chemomet., 14 (2000) 711-723.
[19] M. Zuppa et al., "Recovery of drifting sensor responses by means of DWT analysis", *Sens. Actuat. B: Chem.*, 120(2) (2007) 411-416.
[20] C. Di Natale et al., "Sensor-array calibration time reduction by dynamic modelling", *Sens. Actuat. B: Chem.*, 25(1-3) (1995) 578-583.
[21] O.A. Hammadi, "Characteristics of Heat-Annealed Silicon Homojunction Infrared Photodetector Fabricated by Plasma-Assisted Technique", Phot. Sen., 6(4) (2016) 345-350.
[22] A.Z. Sadek, W. Wlodarski, Y. X. Li, W. Yu, X. Li, X. Yu and K. Kalantar-Zadeh, *Thin Solid Films* 515/24, 8705 (2007).
[23] S.J. Ippolito, S. Kandasamy, K. Kalantar-Zadeh, W. Wlodarski, K. Galatsis, G. Kiriakidis, N. Katsarakis, and M. Suchea, *Sensors and Actuators, B: Chemical* 111–112, 207 (2005).
[24] O.A. Hamadi, "Characterization of SiC/Si Heterojunction Fabricated by Plasma-Induced Growth of Nanostructured Silicon Carbide Layer on Silicon Surface", Iraqi J. Appl. Phys., 12(2) (2016) 9-13.
[25] S. J. Ippolito, S. Kandasamy, K. Kalantar-Zadeh, A. Trinchi, and W. Wlodarski, *Sensor Lett.*, 1/1, 33 (2003).
[26] J. Tan, W. Wlodarski, and K. Kalantar-Zadeh, *Thin Solid Films* 515/24, 8738 (2007).
[27] R. Arsat, S. J. Tan, W. Modarski, and K. Kalantar-Zadeh, *Sensor Lett.* 4, 419 (2006).
[28] J. Yu, S. J. Ippolito, M. Shafiei, D. Dhawan, W. Wlodarski, and K. Kalantar-Zadeh, *Appl. Phys. Lett.* 94/1 (2009).
[29] Y. Shen, T. Yamazaki, Z. Liu, D. Meng, T. Kikuta, and N. Nakatani, *Thin Solid Films* 517/6, 2069 (2009).
[30] O.A. Hammadi, "Effects of Extraction Parameters on Particle Size of Titanium Dioxide Nanopowders Prepared by Physical Vapor Deposition Technique", Plasmonics, 15(6) (2020) 1747-1754.
[31] H. Gong, J. Q. Hu, J. H. Wang, C. H. Ong, and F. R. Zhu, *Sensors and Actuators, B: Chemical* 115/1, 247 (2006).
[32] A. Wisitsoraat, A. Tuantranont, E. Comini, G. Sberveglieri, and W. Wlodarski, *Thin Solid Films* 517/8, 2775 (2009).
[33] E. Comini, G. Sberveglieri, M. Ferroni, V. Guidi, and G. Martinelli, *Sensors and Actuators, B: Chemical* 68/1–3, 175 (2000).
[34] S. T. Shishiyanu, T. S. Shishiyanu, and O. I. Lupan, *Sensors and Actuators, B: Chemical* 107/1, 379 (2005).
[35] M. Oztas and M. Bedir, *Thin Solid Films*, 516/8, 1703 (2008).
[36] J. B. Kim, D. Byun, S. Y. Ie, D. H. Park, W. K. Choi, C. Ji-Won, and A. Basavaraj, *Semicond. Sci. Technol.* 9, 095004 (2008).
[37] G. H. Kim, D. L. Kim, B. D. Ahn, S. Y. Lee, and H. J. Kim, *Microelectron. J.* 40/2, 272 (2009).
[38] K. S. Ahn, T. Deutsch, Y. Yan, C. S. Jiang, C. L. Perkins, J. Turner, and M. Al-Jassim, *J. Appl. Phys.* 102/2, 6 (2007).
[39] H. Xue, Y. Chen, X. L. Xu, G. H. Zhang, H. Zhang, and S. Y. Ma, *Physica E*: Low-dimensional Systems and Nanostructures 41/5, 788 (2009).

IRAQI JOURNAL OF APPLIED PHYSICS
Vol. 18, No. 1, January-March 2022, pp. 31-34

Structural, Morphological and Photoluminescence Characteristics of Cu_2S-Doped Nanostructured ZnS Thin Films Deposited on Porous Silicon

Udar A. Merhan
Tadina B. Simanja

Department of Physics, College of Science, University of Lakshan, Pune, INDIA

In this work, nanostructured zinc sulfide (ZnS) thin films with different contents (2-10 at.%) of copper disulfide (Cu_2S) were prepared by pulsed-laser deposition (PLD) method. The thin film samples with 2, 4 and 6 at.% of Cu_2S showed that the ZnS thin films have wurtzite structure. The peak belonging to the Cu_2S was observed on the x-ray diffraction patterns of the samples containing 8 and 10 at.% of Cu_2S. Furthermore, the x-ray diffraction patterns of porous silicon showed a broadening in the FHWM with increasing etching time. A reduction in the average diameter of the particles with increasing etching time was observed according to the results of atomic force microscopy performed on the prepared samples. The photoluminescence spectra of the porous silicon samples showed that the etching time has a significant effect on the position of UV emission and a blue shift was observed as the etching time was increased from 10 to 50 min.

Keywords: Zinc sulfide; Copper sulfide; Porous silicon; Pulsed-laser deposition
Received: 27 June 2021; **Revised:** 15 January 2022; **Accepted:** 22 January 2022

1. Introduction

Metal sulfide semiconductors such as ZnS, PbS, CdS and Cu_2S [1-5] have attracted significant attention in many various applications due to their simple implementation, low cost, and good reliability for real-time control systems with respect to other similar materials [6]. The employment of metal sulfide semiconductors and their devices is dependent on many factors such as their operating temperatures, morphology and chemical composition [7].

Research into the exploitation of the peculiar optical properties of zinc sulfide started several years ago. Zinc sulfide is one of the most important II-VI compound semiconductors: it has a large (3.6 eV) direct band gap, a sizable exciton binding energy of 39 meV at room temperature [8], and it may in principle support both n- and p-doping. Moreover, ZnS is a low-cost, environmentally benign compound, with convenient mechanical properties, such as good fracture strength and hardness. ZnS exhibits polymorphism since two main crystalline forms can be observed, namely the most stable (below 1290 K) zincblende (ZB) and the high-temperature and synthetically feasible [9] allotrope with wurtzite (WZ) symmetry. ZnS can be transparent in an extremely wide energy range, with a very large transmittance from visible wavelengths to just over 12 micrometers. Indeed, among the many proposed ZnS-based device applications, one can find solar cells, liquid crystal (flat panel) displays, light-emitting diodes and sensors [10-12] transmission windows for visible and infrared optics, due to its optimal performances as optical material. Furthermore, various ZnS-based nanostructures have been successfully synthesized, including nanowires [8,10], nanoribbons [11] and nanotubes [12], that may be easily integrated in nanoscale devices. Among these, particular attention has been payed to nanostructures and multilayers composed of ZnS and its companion ZnO [13], that find relevant applications in piezotronics [14], photovoltaics [15-17] and photodetectors [19]. The combination of ZnS with other materials, such as ZnO, is also strategic in view of novel imaging and sensing applications, e.g. in the field of plasmonics - the main effects being the huge field enhancement and strong localization at the interface - or in the design of hyperbolic metaterials [19], where one exploits the indefinite (hyperbolic) dispersion of the refracted electromagnetic wave.

Copper sulfides have attracted great interest due to their different stoichiometry, complex structure, and unique physical and chemical properties as earth-abundant materials [20-22]. Copper sulfides have several stable solid phases with the stoichiometric compositions varying in a wide range from copper-rich Cu_2S to copper-deficient CuS.

In optoelectronic devices based on metal sulfide semiconductors, the change in the electrical conductivity is attributed to the interaction between the incident photons and the layers within the optical depth on the surface or within the bulk of the metal sulfide semiconductors. Similarly, in gas sensors, for example, the change in the electrical conductivity is due to the interaction of the targeted gas molecules

(chemisorption or physisorption) with the surface of the metal sulfide grains. Consequently, metal sulfide sensors show changes in the resistance under exposure to oxidizing or reducing gases [23]. Since the majority of these sensitive layers are n-type, p-type semiconductors sensitive to gases are highly demanded for gas sensing applications such as sensor arrays for electronic nose [24].

These p-type semiconductor devices have much different operating patterns from their n-type counterparts [25]. In addition, the p-type semiconductors are more appropriate for devices and applications based on the photoresponse, photoconversion, oxidation and reduction processes [26]. At elevated temperatures, the incidence of moderate-energetic photons or the presence of chemically-adsorbed molecules can cause electron depletion at the surface of the metal sulfide grains; and consequently, the electrical resistivity of the thin films increases [2]. The response to the changes in surrounding environment plays an important role in determining the specific interaction on the surface of metal sulfide thin films [27].

The diffusion of copper into ZnS can cause the formation of complex centers (Cu_{Zn}, Cu_i) or replace either substitutionally or interstitially Zn atoms in the ZnS lattice creating structural deformations [28,29]. Copper sulfide significantly affects the electrical, chemical, structural and optical properties of ZnS, and the study of the electronic state of Cu in ZnS has been the subject of interest for a long time [30,31].

2. Experiment

Zinc sulfide powder with different doping concentrations for Cu_2S (2-10 at.%) was pressed under 5 tons to form a target of 2.5 cm in diameter and 0.2 cm in thickness. It should be as dense and homogenous as possible to ensure good quality. The Cu_2S:ZnS thin films with different doping ratios (2, 4, 6, 8 and 10 at.%) were deposited by pulsed-laser deposition (PLD) method inside a 10^{-3} torr evacuated chamber. The focused Q-switched Nd:YAG laser beam is incident at angle of 45° on the target surface. The substrate is placed in front of the target with its surface parallel to that of the target. The film thickness was determined by Spectroscopic Reflectometer SR300 instrument and varied within 100±5nm.

Porous silicon samples were prepared by electrochemical etching where the silicon wafer serves as the anode. The cathode is made of platinum or any HF-resistant and conducting material. A p-type silicon wafer was used as a starting substrate in the photochemical etching. The samples were cut from the wafer and rinsed with acetone and methanol to remove dirt, as well as to remove the native oxide layer on the samples. The electrochemical etching, were carried out in a mixing of HF with ethanol (1:1) with constant current 40 mA and different times (10 and 50 min).

In order to study the structural properties, the crystal structure was analyzed with a Shimadzu 6000 X-ray diffractometer system within the range 20-60°. The morphology of the prepared surfaces was introduced by an atomic force microscope (Angstrom AA3000 Scanning Probe Microscope SPM, tip NSC35/AIBS).

3. Results and Discussion

Figure (1) shows the XRD patterns of Cu_2S-doped ZnS films deposited on Si(111) substrates at different doping ratios (2, 4, 6, 8 and 10 at.%). It can be observed from these patterns that the peaks (31.9403, 34.5121, 36.3949, 47.6923 and 57.0149) refer to (100), (002), (101), (012) and (110) directions, respectively. These patterns coincide with those of the hexagonal structure of ZnS. It can be observed that the peak of Si located at 28.35° is related to (111) crystal plane. The preferred peak of ZnS films doped by 2-10 wt.% Cu_2S ratio appear at 36.39 for (101) plane while the preferred peak of Cu_2S is located at 38.40 for (111) crystal plane. It can be noted that the grain size and d_{hkl} decrease with increasing doping ratio of Cu_2S and the maximum value is observed at doping ratio of 10%.

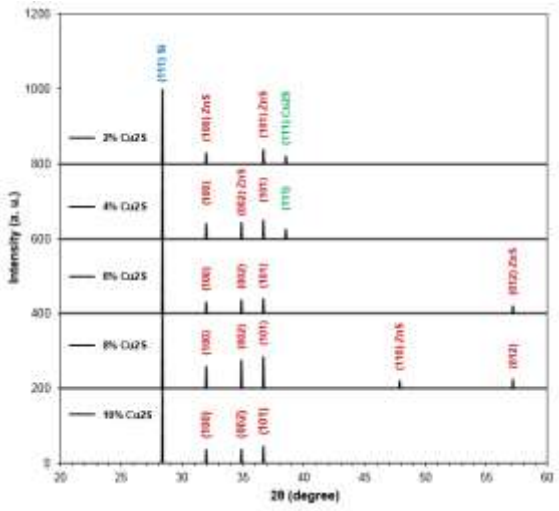

Fig. (1) X-ray diffraction patterns of Cu_2S-doped ZnS films deposited at different doping ratios (2, 4, 6, 8 and 10 wt.%)

Figure (2) shows the XRD patterns of porous p-type Si (111) at different etching times. These patterns show the difference between silicon wafer and porous silicon, where the strong peak of pure Si appears at 28.35 along the (111) direction confirming the monocrystalline structure of the Si layer belonging to the (111) plane of Si cubic structure. Increasing etching time results in broadening of the peak with varying full-width at half maximum (FWHM), as shown in Fig. (2). The thickness of the porous structure is decreasing with increasing etching time and the reduction in the crystallite size can be inferred through the increase in broadening of the XRD spectra.

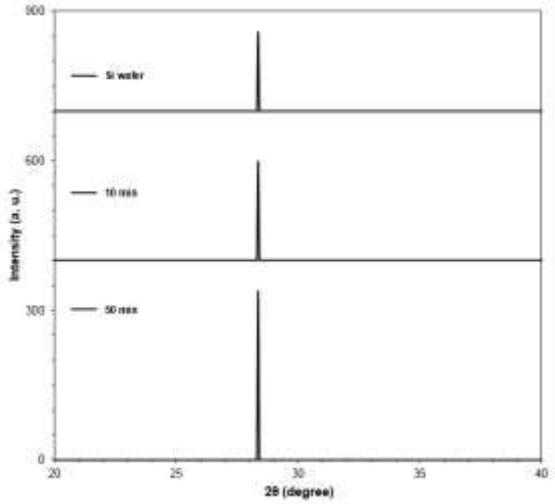

Fig. (2) X-ray diffraction patterns of porous silicon prepared after etching times of 10 and 50 min

Figure (3) shows the AFM images of porous silicon samples prepared after different etching times (10 and 50 min) as the etching current was kept constant at 40 mA. It was observed that the average diameter decreased with increasing etching time and a change in the microstructure of the porous silicon surface is observed at different etching times (10 and 50 min) where the pore size is significantly varied, as shown in the AFM images. This may be caused by inhomogeneous composition of the substrate and electrolyte, and seems to increase with layer thickness.

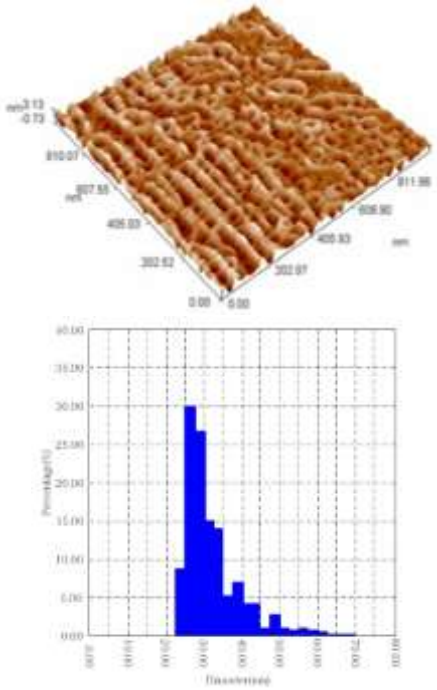

(a)

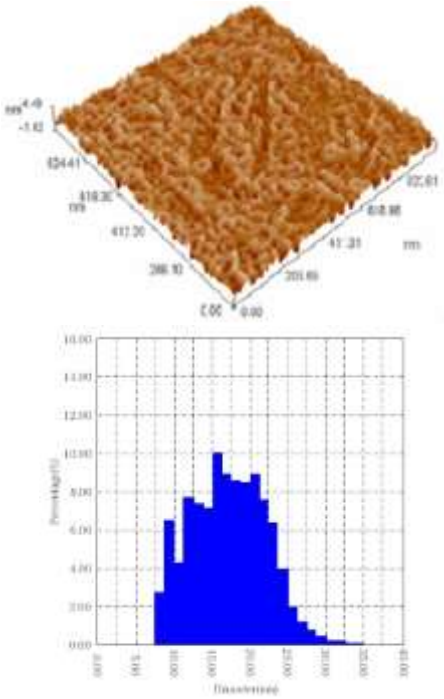

(b)

Fig. (3) AFM images of porous Si wafer prepared at constant current of 40 mA and etching times of 10min (a) and 50min (b)

Figure (4) shows the photoluminescence (PL) spectra of the porous silicon samples prepared after etching times of 10 and 50 min. It is apparent that the exciting wavelength is at 210 nm, which is the maximum absorption peak observed in UV spectra of porous silicon, and the fluorescence spectrum consist of strong UV emission peaks centered at 289 and 291nm for porous silicon prepared at 10 and 50 min, respectively. This blue shift could be attributed to decreasing in grain size.

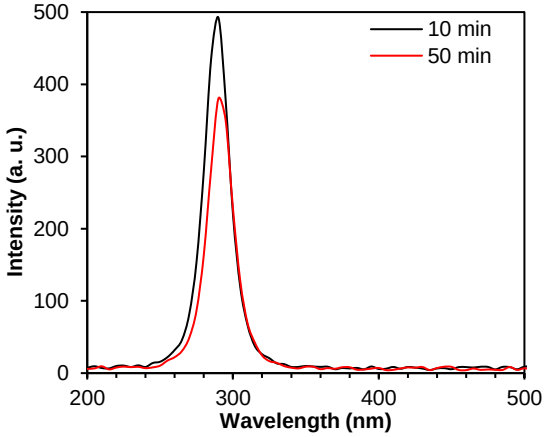

Fig. (4) Photoluminescence (PL) of porous silicon prepared at current of 40 mA and etching times of 10 and 50 min

4. Conclusions

Polycrystalline Cu_2S-doped ZnS structures were successfully prepared as thin films by PLD method. These structures were deposited on the surfaces of porous silicon samples prepared by electrochemical etching method. The topography of porous silicon shows a decrease in average diameter with increasing

etching time. The photoluminescence emission spectrum has a broad blue range with increasing porosity time.

References

[1] A. Z. Sadek et al., *Thin Solid Films* 515/24, 8705 (2007).
[2] S.J. Ippolito et al., *Sensors and Actuators, B: Chemical* 108/1–2, 154 (2005).
[3] S.J. Ippolito et al., *Sensor Lett.*, 1/1, 33 (2003).
[4] J. Tan, W. Wlodarski and K. Kalantar-Zadeh, *Thin Solid Films* 515/24, 8738 (2007).
[5] R. Arsat et al., *Sensor Lett.* 4, 419 (2006).
[6] J. Yu et al., *Appl. Phys. Lett.* 94/1 (2009).
[7] Y. Shen et al., *Thin Solid Films* 517/6, 2069 (2009).
[8] P. Jiang, "Aluminium-doped n-type ZnS nanowires as high-performance UV and humidity sensors", *J. Mater. Chem.*, 22 (2012) 6856-6861.
[9] X. Fang et al., "An efficient way to assemble ZnS nanobelts as ultraviolet-light sensors with enhanced photocurrent and stability", *Adv. Funct. Mater.*, 20 (2010) 500-508.
[10] Y. Jiang et al., "Homoepitaxial growth and lasing properties of ZnS nanowire arrays", *Adv. Mater.*, 18 (2006) 1527-1532.
[11] Y. Jiang et al., "Hydrogen-assisted thermal evaporation synthesis of ZnS nanoribbons on a large scale", *Adv. Mater.*, 15 (2003) 323-327.
[12] S. Farhangfar et al., "Atomic layer deposition of ZnS nanotubes", *Nanotech.*, 20 (2009) 325602.
[13] X. Fang et al., "ZnO and ZnS nanostructures: Ultraviolet-light emitters, lasers, and sensors", *Critic. Rev. Solid State Mater. Sci.*, 34 (2009) 190-223.
[14] S.C. Rai et al., "Piezo-phototronic effect enhanced UV/visible photodetector based on fully wide band gap ZnO/ZnS core/shell nanowire", *ACS Nano*, 9 (2015) 6419-6427.
[15] C. Platzer-Bjorkman et al., "Zn(O,S) buffer layers by atomic layer deposition in Cu(In,Ga)Se_2 based thin film solar cells: band alignment and sulfur gradient", *J. Appl. Phys.*, 100 (2006) 044506.
[16] N. Naghavi et al., "Buffer layers and transparent conducting oxides for chalcopyrite Cu(In,Ga)$(S,Se)_2$ based thin film photovoltaics: present status and current developments", *Prog. Photovolt.*, 18 (2010) 411-433.
[17] J. Chung et al., "Synthesis of a ZnS shell on the ZnO nanowire and its effect on the nanowire-based dye-sensitized solar cells", *J. Phys. Chem. C*, 114 (2010) 21360-21365.
[18] L. Hu et al., "Stacking order dependent optoelectronic properties of bilayer nanofilm photodetectors made from hollow ZnS and ZnO microspheres", *Adv. Mater.*, 24 (2012) 5872-5877.
[19] A. Poddubny et al., "Hyperbolic metamaterials", *Nat. Photon.*, 7 (2013) 948-957.
[20] R. Waser and M. Aono, "Nanoionics-Based Resistive Switching Memories", *Nat. Mater.*, 6(11) (2007) 833-840.
[21] C. Wadia et al., "Materials Availability Expands the Opportunity for Large-Scale Photovoltaics Deployment", *Environ. Sci. Technol.*, 43(6) (2009) 2072-2077.
[22] L. Liu et al., "Thermal Annealing Effects of Plasmonic $Cu_{1.8}S$ Nanocrystal Films and Their Photovoltaic Properties", *J. Phys. Chem. C*, 118(46) (2014) 26964-26972.
[23] O.A. Hamadi, B.A.M. Bader and A.K. Yousif, "Electrical Characteristics of Silicon p-n Junction Solar Cells Produced by Plasma-Assisted Matrix Etching Technique", Eng. Technol. J., 28 (2008).L. A. Obvintseva, *Russian J. General Chem.*, 78/12, 2545 (2008).
[24] A. Wisitsoraat, A. Tuantranont, E. Comini, G. Sberveglieri, and W. Wlodarski, *Thin Solid Films* 517/8, 2775 (2009).
[25] E. Comini, G. Sberveglieri, M. Ferroni, V. Guidi, and G. Martinelli, *Sensors and Actuators, B: Chemical* 68/1–3, 175 (2000).
[26] S. T. Shishiyanu, T. S. Shishiyanu, and O. I. Lupan, *Sensors and Actuators, B: Chemical* 107/1, 379 (2005).
[27] O.A. Hamadi, "Characterization of SiC/Si Heterojunction Fabricated by Plasma-Induced Growth of Nanostructured Silicon Carbide Layer on Silicon Surface", Iraqi J. Appl. Phys., 12(2) (2016) 9-13.
[28] J. B. Kim, D. Byun, S. Y. Ie, D. H. Park, W. K. Choi, C. Ji-Won, and A. Basavaraj, *Semicond. Sci. Technol.* 9, 095004 (2008).
[29] G. H. Kim, D. L. Kim, B. D. Ahn, S. Y. Lee, and H. J. Kim, *Microelectron. J.* 40/2, 272 (2009).
[30] K. S. Ahn, T. Deutsch, Y. Yan, C. S. Jiang, C. L. Perkins, J. Turner, and M. Al-Jassim, *J. Appl. Phys.* 102/2, 6 (2007).
[31] H. Xue, Y. Chen, X. L. Xu, G. H. Zhang, H. Zhang, and S. Y. Ma, *Physica E*: Low-dimensional Systems and Nanostructures 41/5, 788 (2009).

IRAQI JOURNAL OF APPLIED PHYSICS
Vol. 18, No. 1, January-March 2022, pp. 35-38

Fluorescence Characteristics of Coated-Cell Dye Solutions Containing Highly-Pure Nanoparticles as Random Gain Media

Murad R. Hashem
Mohammed A. Hameed

Department of Physics, College of Science, University of Baghdad, Baghdad, IRAQ

In this work, enhancement to the fluorescence characteristics of laser dye solutions hosting highly-pure titanium dioxide nanoparticles as random gain media. This was achieved by coating two opposite sides of the cells containing these media with nanostructured thin films of highly-pure titanium dioxide. Two laser dyes; Rhodamine B and Coumarin 102, were used to prepare solutions in hexanol and methanol, respectively, as hosts for the nanoparticles. The nanoparticles and thin films were prepared by dc reactive magnetron sputtering technique. The enhancement was observed by the narrowing of fluorescence linewidth as well as by increasing the fluorescence intensity. These parameters were compared to those of the dye only and the dye solution hosting nanoparticles without coatings on the cell. For Rhodamine B and Coumarin 102 samples, the fluorescence intensity of coated-cell sample was increased by 230, and 351%, respectively, with respect to that of dye only and by 152 and 141%, respectively, with respect to that of uncoated cells. The full-width at half-maximum (FWHM) was determined for both cases and found to be 8 and 9 nm, respectively.

Keywords: Laser dye; Random gain media; Rhodamine B; Coumarin 102
Received: 28 December 2021; **Revised:** 08 February 2022; **Accepted:** 15 February 2022

1. Introduction

The importance of organic dyes and pigments in spectral, environmental and industrial applications is increasing significantly due to many modern uses that have emerged during the past two decades [1-5] and the wavelength of the emitted light necessarily represents the difference in energy between these levels [6-8]. The uses and applications of lasers are also radical. The need for laser emission increases at very specific wavelengths [9,10]. Random gain modes made it easy to produce a laser emission at a given wavelength without any additional components or optical elements [11,12]. This mainly depends on the choice of host (dye) and dispersed particles (dispersants) and their spectral properties [13-15].

When nanoparticles are used as dispersants in the host medium, the wavelength of laser emission is limited by the similar interaction of these particles with radiation as they can be considered as similar quantum entities [16,17]. In fact, the differences in such interactions are too small to produce a wide range of laser wavelengths [18].

Recently, a laser emission with a width of 4 nm has been produced [19]. Reducing the complexities of the system and thus the cost of random laser production should be reasonably large to replace the traditional sources of narrow linear lasers, especially tunable dye and diode lasers [20]. Otherwise, some advantages of conventional lasers cannot be compensated [21].

In this work, enhancement to the fluorescence characteristics of laser dye solutions hosting highly-pure titanium dioxide nanoparticles as random gain media. This is achieved by coating two opposite sides of the cells containing these media with nanostructured thin films of highly-pure titanium dioxide. Two laser dyes; Rhodamine B and Coumarin 102, are used to prepare solutions in suitable solvents as hosts for the nanoparticles. This enhancement is observed by the narrowing of fluorescence linewidth as well as by increasing the fluorescence intensity.

2. Experimental Method

Two laser dyes. Rhodamine B and Coumarin 102 (from Lambda Physik) were prepared in this work using the preparation and dilution equations. The dye solution was prepared by dissolving different molar concentrations of each dye (10^{-2}, 10^{-3}, $5x10^{-4}$, 10^{-4}, $5x10^{-5}$, 10^{-5}, 10^{-6}M) in different solvents (hexanol and methanol) at the same concentration,10^{-2} Prepared only and not used in tests, whether absorbance or fluorescence, to reduce the error rate when preparing with dilution and preparation equations. Absorption and flash spectra were recorded to determine the optimal concentration and solvent. We considered that 5×10^{-5} M concentration was the best for rhodamine B dye dissolved in hexanol and 10^{-4} was

the best concentration for Coumarin dye 102 dissolved in methanol as an ideal sample for both dyes. High purity argon gas was used to generate the plasma column by glowing discharge between two electrodes (anode and cathode) while high purity oxygen gas was used as reaction gas with a mixing ratio ($Ar|O_2$) of 50:50 and a total gas pressure of 0.1 mbar. Thin films of nanocomposite titanium dioxide were prepared using a dc reactive magnetron spraying technique and deposited on glass cells placed on the anode. Film thickness was controlled by deposition time as the electrode distance between cathode and anode in the vacuum plasma system remained constant (4 cm). A cooling system was used to cool the discharge electrodes in order to prevent secondary electron emission from the cathode as well as to prevent heat-induced growth of large particles at the anode. More details on this system can be found elsewhere [22-25]. The titanium dioxide nanoparticles were extracted as nanopowder from thin-film samples using a new technique known as ultrasound-assisted extraction with simultaneous freezing. In this technique, nanoparticles are extracted from the thin film without any heat treatment or mechanical processing, thus no particle size increase occurs [25,26].

The spectrophotometric properties of the dye solutions were determined by a computer-controlled K-MAC SpectraAcademy SV-2100 UV-visible spectrophotometer in the spectral range 200-800nm and fluorescence spectra were recorded with a F96 spectrophotometer unit (Shanghai LengGuang Technique. Co., Ltd.) in the spectral range of 180-900 nm with a 532 nm laser as the excitation source. The laser output was recorded using a fast high-resolution detector (CCD) connected to an RS232 card storage oscilloscope. Highly-pure titanium dioxide nanoparticles were added to the dye solution in different amounts (0.5, 1, 1.5, 2 and 2.5 mg) with slow stirring to ensure the diffusion of these nanoparticles into the dye solution, and the final sample was made for the random-gain medium of rhodamine B and Coumarin 102 by adding titanium dioxide to the dye solution inside the titanium-coated glass cell on two opposite sides, which is as shown in Fig (1), in which the fluorescence of the prepared samples are visually clear on the right side of both photographs.

Despite the fact that nanoparticles may precipitate to the bottom of the glass tube, measurements confirmed that nanoparticles were randomly distributed in the dye liquid medium and their number was large enough to perform polydispersity.

3. Results and Discussion

Figure (2) shows the fluorescence spectra of Rhodamine B and Coumarin 102 dyes in hexanol and methanol, respectively, for dye solution only, dye solution hosting the nanoparticles, and dye solution hosting the nanoparticles with two opposite sides of the cell containing the solution coated with TiO_2 thin films. A 532 nm laser source was used to irradiate the samples in order to measure the fluorescence spectra.

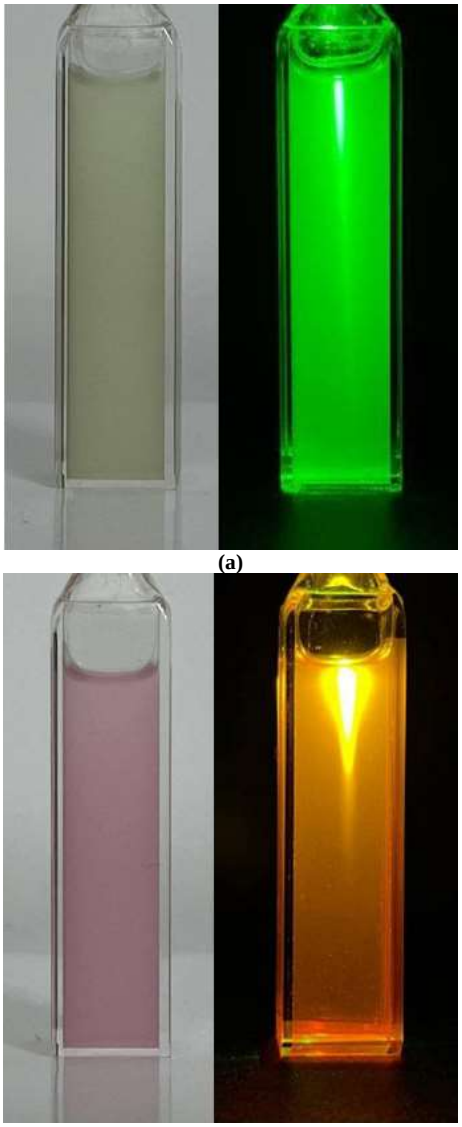

Fig. (1) (a) Rhodamine B dye solution in hexanol hosting 2.5 mg of TiO_2 nanoparticles, and (b) Coumarin 102 dye solution in methanol hosting 2.5 mg of TiO_2 nanoparticles. In both cases, the quartz cells containing the samples were coated on two opposite sides with nanostructured TiO_2 thin films

The fluorescence spectrum of Rhodamine B dye only (Fig. 2a) shows a broad peak of 520-610 nm with FWHM of 50 nm. The fluorescence spectrum of dye solution hosting the highly-pure TiO_2 nanoparticles shows reasonably higher intensity and FWHM of 17 nm. This is attributed to the role of TiO_2 nanoparticles as scattering centers through the dye solution. This is the concept of random gain medium formed from dye solution hosting nanoparticles. Similar behavior is observed for the Coumarin 102 dye but the peak of the fluorescence spectrum lies within 500-570 nm and approximately centered at 534 nm and the FWHM is 15 nm after adding the nanoparticle to the dye solution. The effect of TiO_2 film coatings on two

opposite sides of the quartz cell on the fluorescence spectra of Rhodamine B and Coumarin 102 dye samples is observed by the further increase in the intensity of fluorescence spectrum and the decrease in the FWHM to be 8 and 9 nm, respectively. These results are summarized in Table (1).

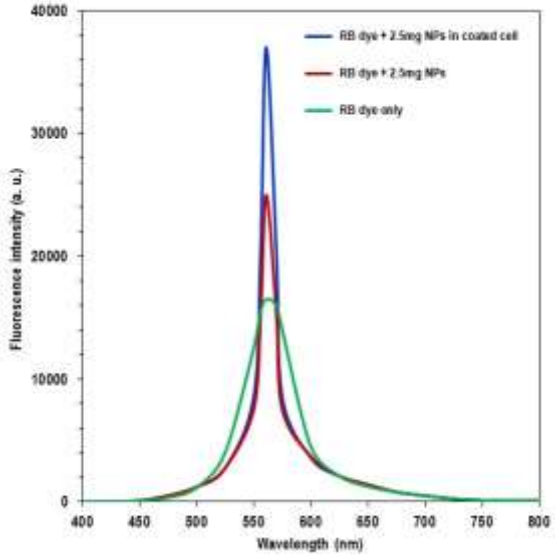

(a)

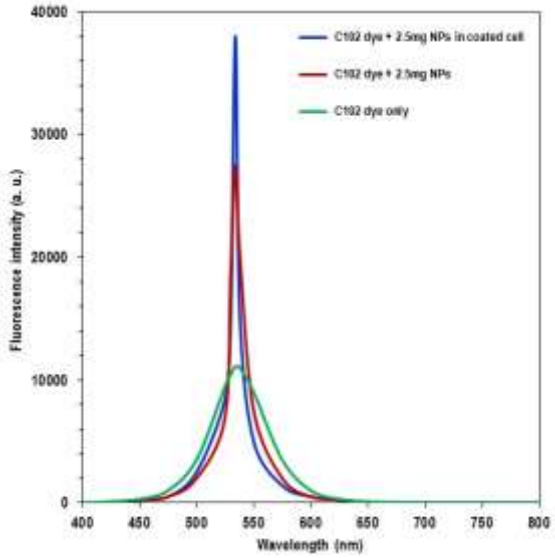

(b)

Fig. (2) Fluorescence spectra of (a) Rhodamine B and (b) Coumarin 102 dye solutions in hexanol and methanol, respectively, hosting 2.5 mg of TiO_2 nanoparticles and the quartz cells containing the samples were coated on two opposite sides with nanostructured TiO_2 thin films

Table (1) Output parameters of the random lasers fabricated in this work

Sample	Peak wavelength (nm)	Peak intensity (a. u.)	FWHM (nm)
Rhodamine B	561	38000	8
Coumarin 102	534	39000	9

It is apparent that the difference in intensity and FWHM between the two cases is not large enough to prefer one dye over the other. Therefore, the peak wavelength is the criterion to choose the suitable dye for certain spectral range.

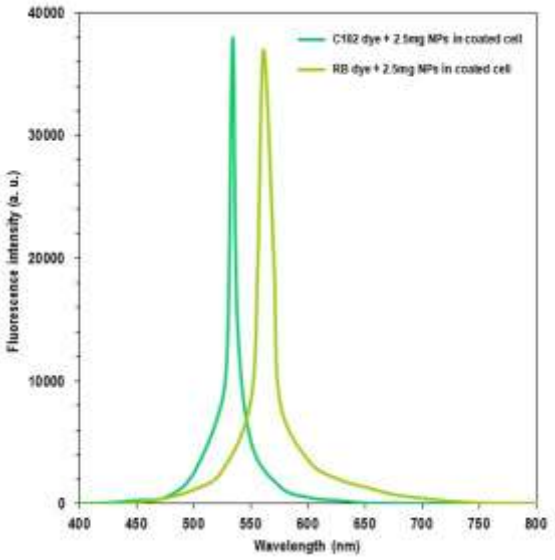

Fig. (3) Comparison of fluorescence spectra of Rhodamine B and Coumarin 102 dye solutions in hexanol and methanol, respectively, hosting 2.5 mg of TiO_2 nanoparticles and the quartz cells containing the samples were coated on two opposite sides with nanostructured TiO_2 thin films

4. Conclusions

In the concluding remarks a random gain medium was synthesized to produce a laser beam in the green region of the electromagnetic spectrum (529-531 nm). These media were made from a dye solution containing high-purity titanium dioxide nanoparticles. The narrow emission line width was determined using FWHM at about (9) nm for titanium dioxide nanoparticles in Rhodamine B dye solution, while FWHM was (8) nm for these nanoparticles in Coumarin dye solution 102. Where we note that when adding titanium dioxide particles The top changed and became narrower. Also, when coating the glass cell with titanium dioxide, the intensity increases and the thickness of the top decreases, and this indicates an increase in the effective medium clearly. This is a very encouraging attempt to achieve high-efficiency manufacturing and the low cost of laser random transfer in the visible area.

References

[1] M. Maeda, **"Laser Dyes, Properties of Organic for Dye Laser"**, Academic Press, Inc., (1984).
[2] W. Demtroder, **"Laser Spectroscopy"**, Springer-Verlag (New York, 1981), 330-350.
[3] H. Cao et al., "Random laser action in semiconductor powder", *Phys. Rev. Lett.*, 82(11) (1999) 2278-2281.
[4] S.K. Turitsyn et al., "Random distributed feedback fibre lasers", *Phys. Rep.*, 542(2) (2014) 133-193.
[5] H. Ramachandran, "Mirrorless lasers", *Pramana J. Phys.*, 58(2) (2002) 313.

[6] S. Wiersma, "The physics and applications of random lasers", *Nature Phys.*, 4 (2008) 359-365.
[7] D.V. Churkin et al., "Recent advances in fundamentals and applications of random fiber lasers", *Adv. Opt. Photon.*, 7 (2015) 516-569.
[8] P. Sebbah and C. Vanneste, "Random laser in the localized regime", *Phys. Rev. B*, 66 (2002) 144-202.
[9] J. Andreasen et al., "Modes of random lasers", *Adv. in Opt. Photon.*, 3(1) (2011) 88-127.
[10] R.C. Polson and Z.V. Vardeny, "Random lasing in dye-TiO_2 solution and π conjugated polymer films", *Phys. B*, 338 (2003) 219-223.
[11] A.A.R. Mahmood, O.A. Hammadi and K.R. Ibraheem, "Some Physical Properties of Metal-Hydroxyquinoline Complexes in Different Solvents", Iraqi J. Appl. Phys., 17(1) (2021) 9-16.
[12] S. John and G. Pang, "Theory of Lasing in a Multiple Scattering Medium", *Phys. Rev. A*, 54(4) (1996) 3642.
[13] A. Ishimaru, **"Wave propagation and scattering in random media"**, Academic Press (New York, 1978) 175-183.
[14] M.A. Hameed, "Effects of Solvent Properties on Absorption and Fluorescence Characteristics of Two Organic Dyes Used as Random Gain Media", *Iraqi J. Appl. Phys.*, 17(2) (2021) 15-18.
[15] P. Sebbah, B. Hu and A.Z. Genack, "Speckle analysis of the microwave field in transmission through random media", *Proc. SPIE*, 6341 (2006), Speckle06: Speckles, From Grains to Flowers, 63411E.
[16] A.J.C. Kuehne and M.C. Gather, "Organic Lasers: Recent Developments on Materials, Device Geometries, and Fabrication Techniques", *Chem. Rev.*, 116(21) (2016) 12823-12864.
[17] F.J. Duarte, "Liquid and solid-state tunable organic dye lasers for medical applications", in **"Lasers for Medical Applications"**, Woodhead Publishing (2013) 203-221.
[18] J. Kitur et al., "Dependence of the random laser behavior on the concentrations of dye and scatterers", *J. Opt.*, 12(2) (2010) 024009.
[19] B.K. Nasser and M.A. Hameed, "Narrow Emission Linewidth of Highly-Pure Silicon Nitride Nanoparticles in Different Dye Solutions as Random Gain Media", *Nonl. Opt. Quant. Opt.: Concepts in Modern Optics*, 53(1-2) (2021) 99-105.
[20] H.G. Fahad and O.A. Hammadi, "Characterization of Highly-Pure Silicon Dioxide Nanoparticles as Scattering Centers for Random Gain Media", Iraqi J. Appl. Phys., 16(2) (2020) 37-42.
[21] D. Magde, R. Wong and P.G. Seybold, "Fluorescence Quantum Yields and Their Relation to Lifetimes of Rhodamine 6G and Fluorescein in Nine Solvents: Improved Absolute Standards for Quantum Yields", *Photochem. Photobio.*, 75(4) (2002) 327-334.
[22] F.J. Al-Maliki, O.A. Hammadi and E.A. Al-Oubidy, "Optimization of Rutile/Anatase Ratio in Titanium Dioxide Nanostructures prepared by DC Magnetron Sputtering Technique", *Iraqi J. Sci.*, 60(special issue) (2019) 91-98.
[23] F.J. Al-Maliki and E.A. Al-Oubidy, "Effect of gas mixing ratio on structural characteristics of titanium dioxide nanostructures synthesized by DC reactive magnetron sputtering", *Phys. B: Cond. Matter*, 555 (2019) 18-20
[24] R.A.H. Hassan and F.T. Ibrahim, "Preparation and Characterization of Anatase Titanium Dioxide Nanostructures as Smart and Self-Cleaned Surfaces", *Iraqi J. Appl. Phys.*, 16(4) (2020) 13-18.
[25] Mohammed A. Hameed, Saja H. Faisal, Reem H. Turki, "Characterization of Multilayer Highly-Pure Metal Oxide Structures Prepared by DC Reactive Magnetron Sputtering Technique", *Iraqi J. Appl. Phys.*, 16(4) (2020) 25-30
[26] O.A. Hammadi, "Production of Nanopowders from Physical Vapor Deposited Films on Nonmetallic Substrates by Conjunctional Freezing-Assisted Ultrasonic Extraction Method", *Proc. IMechE, Part N, J. Nanomater. Nanoeng. Nanosys.*, 232(4) (2018) 135-140.
[27] O.A. Hammadi, "Effects of Extraction Parameters on Particle Size of Titanium Dioxide Nanopowders Prepared by Physical Vapor Deposition Technique", *Plasmonics*, 15(6) (2020) 1747-1754.

THE IRAQI JOURNAL OF APPLIED PHYSICS
EDITORIAL BOARD

COPYRIGHT RELEASE FORM
IRAQI JOURNAL OF APPLIED PHYSICS (IJAP)

We, the undersigned, the author/authors of the article titled

……
……
……
……
……
……
……

that is submitted to the Iraqi Journal of Applied Physics (IJAP) for publication, declare that we have neither taken part or full text from any published work by others, nor presented or published it elsewhere in any other journal. We also declare transferring copyrights and conduct of this article to the Iraqi Journal of Applied Physics (IJAP) after accepting it for publication.

The authors will keep the following rights:

1. Possession of the article such as patent rights.
2. Free of charge use of the article or part of it in any future work by the authors such as books and lecture notes after informing IJAP editorial board.
3. Republishing the article for any personal purposes of the authors after taking journal permission.

To be signed by all authors:

Signature:……..date: ……
Printed name: ……

Signature:……..date: ……
Printed name: ……

Signature:……..date: ……
Printed name: ……

Correspondence
address:……...
……
Address:……
……
Telephone:……..……email: ……

Note: Complete and sign this form and mail it to the below address with your finally revised manuscript

The Iraqi Journal of Applied Physics
www.iraqiphysicsjournal.com
Email: info@iraqiphysicsjournal.com
Email: editor_ijap@yahoo.co.uk
Email: irq_appl_phys@yahoo.com

IRAQI JOURNAL OF APPLIED PHYSICS

Volume (18), Issue (1), January-March 2022

CONTENTS